UNIVERSITY OF OKLAHOMA

GRADUATE COLLEGE

3D RESERVOIR GEOMECHANICS MODEL OF THE PROPOSED FORGE LABORATORY SITE NEAR MILFORD UTAH

A THESIS

SUBMITTED TO THE GRADUATE FACULTY

in partial fulfillment of the requirements for the

Degree of

MASTER OF SCIENCE

By

MICHAEL JANIS
Norman, Oklahoma
2018

3D RESERVOIR GEOMECHANICS MODEL OF THE PROPOSED FORGE LABORATORY SITE NEAR MILFORD UTAH

A THESIS APPROVED FOR THE
MEWBOURNE SCHOOL OF PETROLEUM AND GEOLOGICAL
ENGINEERING

BY

Dr. Ahmad Ghassemi, Chair

Dr. Xingru Wu

Dr. Matthew Pranter

Acknowledgements

I thank my advisor Dr. Ahmad Ghassemi for his help, support, and advice throughout my time at the university of Oklahoma. I have very much enjoyed my time working with him and look forward to a continued professional relationship. His flexibility and patience have made my time at OU successful and memorable.

I also thank Dr. Robert Podgorney with the Idaho National Lab for his generous mentorship and financial support of my education. His involvement in my research has provided me with unique perspectives on research and the energy industry.

I thank Zhi Ye for sharing and passing on to me his knowledge of experimental rock mechanics. I very much enjoyed and appreciate our collaboration efforts.

I thank the members of my committee, Dr. Matthew Pranter and Dr. Xingru Wu for donating their time and expertise to review and provide advice for my thesis work.

Finally, I thank the faculty and staff of the Mewbourne School of Petroleum and Geological Engineering for their hard work and contribution to my educations and many others'.

Table of Contents

List of Tables

List of Figures

Abstract

3-D mechanical earth models provide an effective means of reservoir characterization and reducing risks in reservoir development. A mechanical earth model is composed of a structural model, a 3D property model, a DFN, and a stress model. The structural geologic model is subdivided based on mechanical stratigraphy. The 3D property model is the result of interpolating well data inside the structural framework. The DFN is created to represent the distribution and properties of in-situ fractures. The stress model is developed using regional and local data. Mechanical earth models reduce risk associated with drilling by informing casing set point decisions and stimulation by providing estimates of stress magnitudes and rock properties.

In this thesis a 3D mechanical earth model is constructed for the FORGE laboratory site near Milford Utah. The site resides on the western side of the Mineral Mountains approximately 3 km west of an existing geothermal power plant. The Mineral Mountains are composed of a series of intrusive plutons and the rocks at reservoir depth are granites and grano-diorites. The modeling procedure began with creating a structural geologic model and incorporating existing known faults and their impact on different geologic units in the reservoir. All available data to date indicate no discernible fault offsets in the model area.

Then 1-D mechanical models were developed along existing wells. Well logs from the five (5) deep wells near the site were used to calculate the overburden, Young's modulus, Poisson's ratio, and rock strength along the wellbores. Empirical correlations were used to determine rock strength from compressional sonic logs, to estimate shear slowness where not available, and to correlate between static and dynamic properties.

The correlations were calibrated with data from several triaxial tests performed on samples from reservoir depths (6000 – 7500 ft). The mechanical data were then used as input to estimate the horizontal stresses using the strain corrected version of the Poisson's relation (Blanton et al., 1997), breakout analysis using Kirsch's equation (elasticity theory), and faulting theory. Horizontal stresses were found to be very close in magnitude since the granite tends to be isotropic and the MU-ESW1 well logs show fast and slow shear velocities are less than 5% different most of the logged granite range (Figure 20). The structural model was then populated with the 1-D mechanical models. The reservoir stress orientations were considered to be consistent with the regional direction as indicated by the normal faulting associated with E-W extension. The maximum horizontal stress strikes north-northeast and south-southwest. Finally, A discrete fracture network (DFN) was created using Mangrove in Petrel software. Fracture data along the newly drilled MU-ESW1 were found to group into different sets based on strike and dip (Figure 39) and were used to create a stochastic fracture model. The resulting structural model populated with the 1-D MEMs, stress estimates and an associated discrete fracture model constitute the 3-D Mechanical Earth Model and provide valuable data for stimulation models of the site.

Chapter 1 Introduction

1.1 Introduction to EGS

Enhanced geothermal systems (EGS) have received increasing attention as a renewable and green energy source and are a focus of the US department of energy, GTO (Geothermal Technology Office). The concept of EGS has been around for quite some time with extensive financial and academic efforts dedicated to sites such as Rosemanowes, Fenton Hill and Basel. Enormous energy reserves are estimated to lay in this resource (Tester et al., 2006). EGS reservoirs are located in hot and often dry rocks with very low permeability. The rocks are typically granite, however, some EGS reservoirs occur in certain sedimentary units such as the lower Triassic rocks of central Poland (Bujakowsi et al., 2015; Sowizdzal et al., 2013) and the upper Permian of the North German Basin (Schellschmidt et al., 2010). Typically, the geology near heat sources is granitic or metamorphosed rocks, however, there is significant interest in applying the EGS model to certain depleted oil and gas reservoirs which can have significant temperatures and cheaper development costs due to existing wells (Blackwell et al., 2006). The objective when selecting EGS sites is to find a hot rock mass in an area close to water resources and power infrastructure. In practice, the candidate rocks tend to have some natural fractures and very little to no porosity to allow control for water circulation for heat extraction. The natural fractures can be sealed with calcite (common in geothermal fields) or simply closed due to stresses. Flow paths to facilitate heat transfer are then created by hydraulically stimulating the rock mass and creating new fractures and/or causing shear stimulation (Pine and Batchelor, 1984; Willis-Richards et al., 1996; Baria et al., 1999; Rahman et al., 2002;

Nygren and Ghassemi, 2005; Cheng and Ghassemi, 2016s; Ye et al., 2017) on existing fractures or some other means. Water is then circulated through the stimulated reservoir volume from an injection well to a production well where it is produced, and the fluid is flashed to steam to turn turbines or the heat is used to flash a secondary fluid to steam which is then used to drive turbines.

1.2 Introduction to MEM

The use of Mechanical earth models has seen increased interest in the oil and gas industry as a means of reducing risks associated with drilling, casing, stimulation, and production (Afsari et al., 2009; Plumb et al., 2000; Spence et al., 2014; Barton et al., 2013; Zoback, 2010; Liu, 2017; Hemami and Ghassemi, 2018). These same risks apply to the geothermal sphere as well. Geothermal wells for EGS sites are frequently drilled in challenging environments (e.g., Newberry, Fenton Hill) where severe under pressure zones and formation breakdown and sloughing plague drilling operations. Mechanical models and well drilling models can help to identify and mitigate drilling related problems such as these by helping determine casing shoe set points, mud weight and viscosity. The Rosemanowes experiment was designed to test stimulation methods such as shear stimulation using water injection and proppant placement. Knowledge of in-situ stresses, fracture network orientations and rock strengths would greatly benefit such stimulation operations. The site at Basel, Switzerland suffered from an accidental fault reactivation (Kraft et al., 2009). Knowledge of in-situ stresses, porosity, fracture networks, and pore pressure help prevent this type of problem.

Adequate knowledge of fracture network flow and transport characteristics is necessary to ensure production sustainability. For this, one needs strength and deformation properties of natural fractures. This is particularly the case when stimulation reactivates healed fractures in contrast to initiating a new hydraulic fracture in intact rock (most rocks tend to have higher tensile strength than the material sealing the joint within them). Attempted hydraulic fracture operations in an environment with few natural fractures or a few dominant fractures can cause short circuiting of the system and significant reduction in heat transfer potential as happened at Fenton hill (Brown et al., 2012).

1.3 FORGE Milford Site Geologic Setting

1.3.1 Structure and Stratigraphy

The FORGE laboratory site is located near Milford, Utah just west of the Blundell Power Plant in Milford Valley (Figures 1 and 2). Many previous researchers have focused their efforts on developing conceptual hydrological and geological models of the site because of its geothermal potential. The presence of the Roosevelt hot springs confirms a heat source under the mineral mountains which researchers and DOE officials have long hoped to tap into for EGS experiments. Nielson et al (1986) developed a conceptual model of the site to explain the plutonism and dike intrusion. Several geologic mapping efforts of the area have been undertaken (Hardwick et al., 2016; Nielson et al., 1986; Ross et al., 1982; Coleman et al., 1997; Gertson and Smith 1979). The key structures in the site are the Negro Mag fault which strikes roughly EW and the opal mound fault which strikes NE-SW shown in Figures 1 and 2. Numerous temperature models have been constructed for the site indicating that the required temperatures of 175 C are present at reservoir depth (Gwynn et al., 2016).

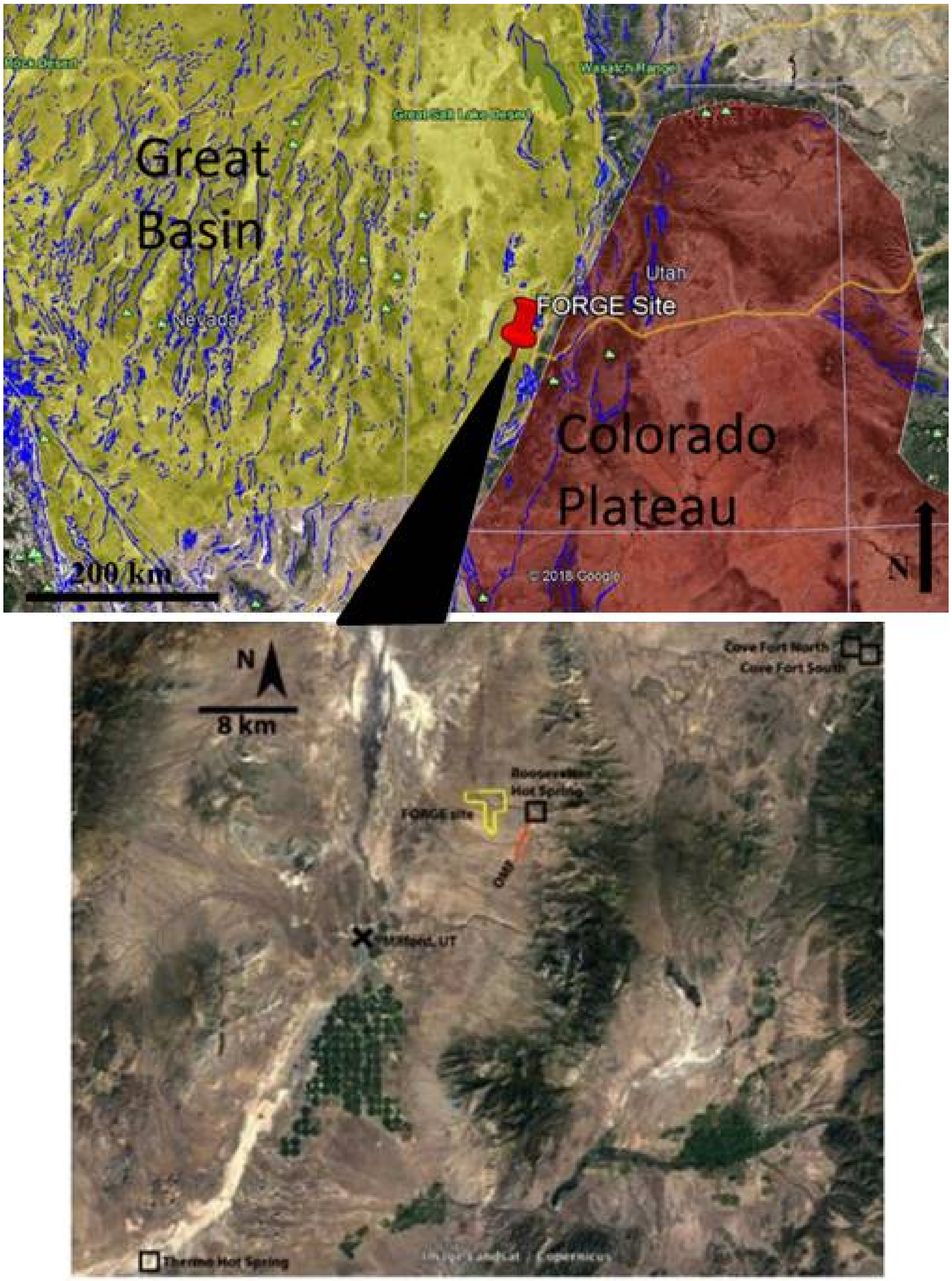

Figure 1: Top: FORGE site regional location, mapped faults shown in blue (Google maps, May, 2018; faults downloaded from USGS in KML format May, 2017). Bottom FORGE site local location (yellow), Roosevelt Hot Springs (black square next to FORGE site) and Opal Mound fault (red line) (EGI, 2018)

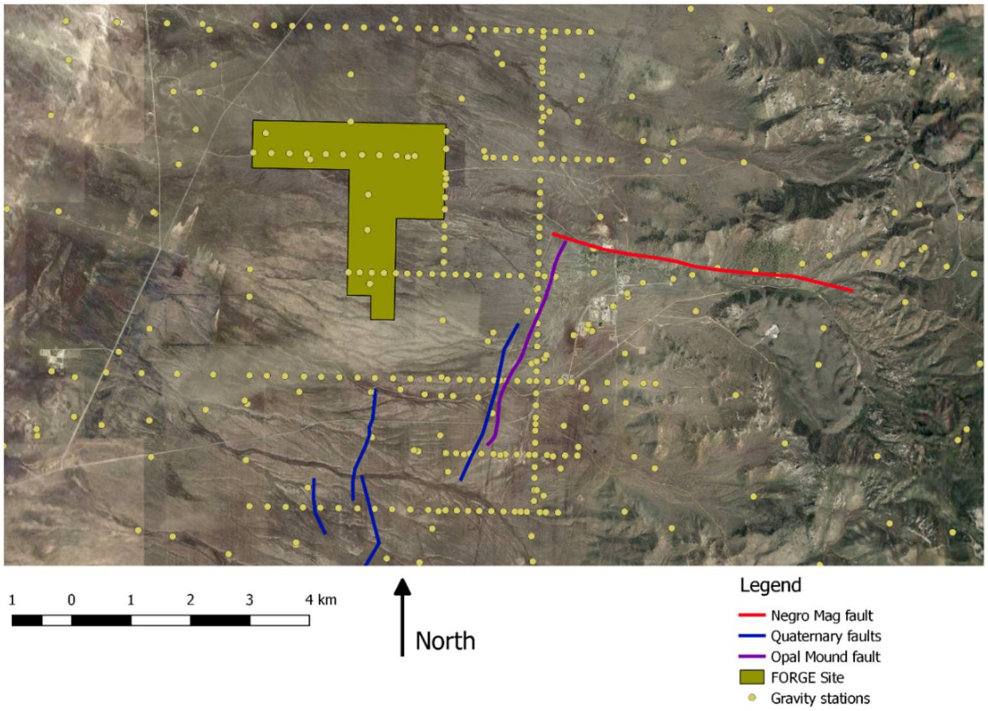

Figure 2: Closer view of FORGE site (shaded area) showing gravity collection stations (yellow points), Negro Mag fault (red line), Opal Mound fault (purple line) and faults cutting only sediments (blue lines) (Bing maps, July, 2017)

1.3.2 Previous Reservoir Geomechanics Work

Despite efforts to assess certain geological and geomechanical aspects of the area, no systematic effort has been devoted to developing a 3D MEM. Several researchers have explored the regional stress state and the structure of the current FORGE site. Arabasz and Julander (1986) found the least principal stress in the mineral mountains area to be oriented at an azimuth of about 102 degrees. Nielson (1989) proposed that based on the observations the stresses in the RHS have to be different than regionally and that the opal mound structure acts as a mechanism of structural decoupling from the regional stress field. Faulder (1994) suggested that the Opal mound fault acts as a dam containing geothermal fluids within the RHS field and causing pressure to drop westward. Keys (1979) used breakout analysis in an unnamed well believed to be 14-2 to determine the orientation of the mid principal stress (max horizontal) to be about 035 degrees. Keys (1979) also observed a multitude of fractures in the acoustic image logs with similar orientations to observed normal faults. Bruhn et al. (1982) conducted a thorough study of joints and fractures in the Mineral Mountains and developed a failure envelope (Figure 3) for the mineral mountains granite based on tensile strength tests they conducted, and compressional strength tests conducted by Pratt and Simonson (1976). Several other researchers have focused efforts on well log data and seismic data to constrain stress directions. However, no integrated 3-D mechanical and structural modeling efforts have been completed to date.

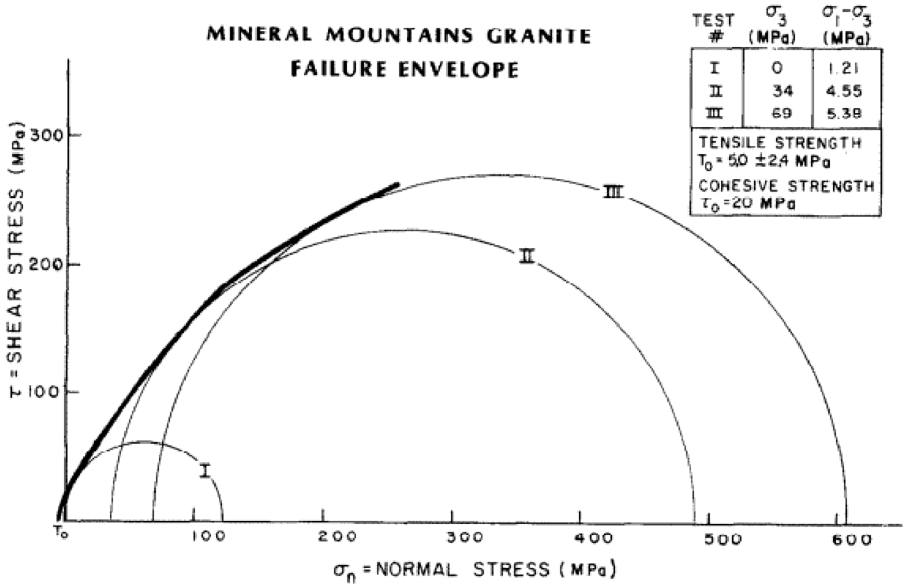

Figure 3: Failure envelope for granites of the mineral mountains (Bruhn et al., 1982)

1.4 Scope of This Work

This thesis will integrate all previous structural geology theories and data with newly acquired data and mapping efforts to create a 3-D structural model of the FORGE site. The structural model is then gridded with a 3-D simulation grid designed to capture the appropriate amount of reservoir detail. This model will then be used to create a 3-D mechanical earth model by populating the structural model and simulation grid with 1-D Mechanical models containing properties measured and correlated from well logs such as neutron porosity, density, sonic compressional and shear slowness, etc. Stress directions will then be estimated from FMI log data revealing drilling induced fractures. Stress magnitudes will be estimated by combining elasticity methods and faulting theory to obtain better constrained values calibrated to field data. The final step to creating a MEM is to create stochastic discrete fracture networks (DFN) in the reservoir rock for each apparent fracture set. These networks can be up-scaled to the simulation grid as porosity and/or exported for use in other simulation software. The combination of these three models (structural, mechanical, and fracture) will constitute the 3-D MEM of the Milford FORGE site. The model constructed herein is approximately 8 km by 8 km in aerial extent and is intended primarily to generate inputs for thermal modeling applications and to provide 3D visualizations of regional stresses, structures and properties.

Chapter 2 Theories and workflow

2.1 The Reservoir In-Situ Stress State

When direct measurements are not available, usually two theories are applied to the problem of stress magnitude estimation: Elasticity theory and faulting theory. Elasticity theory encompasses multiple methods while faulting theory is applied using one method. Elasticity is used to estimate horizontal stress due to elastic deformation caused by the overburden and pore pressure. It is most applicable in quiescent basins where the Poisson effect is the dominant contributing factor to horizontal stresses. At times, it can produce reasonable estimates in seismically active areas as well but must be constrained to faulting theory. Faulting theory applies the Mohr Coulomb envelope to crustal/reservoir rocks to obtain estimates of the minimum or maximum horizontal stress magnitudes for various (faulting) stress regimes. Faulting theory best applies in seismically active areas. These methods are applied up to depths below a few hundred meters below the ground surface where stresses are not affected by erosion, and topography, glaciations, etc.

2.1.1 Faulting Theory: Limiting Stress Ratio

Faulting theory can be applied in tectonically active regions to constrain the lower limit of the minimum principal stress or the upper limit of the maximum principal stress (Jaeger et al., 1978; Moos and Zoback 1990). It assumes that fracture planes ideally oriented with respect to the maximum and minimum principal stresses already exist and the only resistance to slip is friction. This is expressed using the Mohr-Coulomb criterion written in terms of friction in equation (2-1) and in terms of phi in equation (2-2). Both equations exclude rock strength since they are describing pre-existing fault planes:

$$\frac{\sigma_v - P_p}{\sigma_h - P_p} = \left((1 + \mu^2)^{\frac{1}{2}} + \mu\right)^2 \qquad (2-1)$$

$$\left(\sigma_1 - P_p\right) = (\sigma_3 - P_p)\tan^2\left(45 + \frac{\varphi}{2}\right) \qquad (2-2)$$

Roughness of the joints is excluded since they are assumed to be active faults with gouge in the place of asperities. The greatest principal stress is usually taken to be the overburden, σ_v . This is calculated by integrating the density logs (which have been calibrated with core data) though it can be estimated if reliable density log data is not available. The least principal stress, σ_h, is usually the least horizontal stress. The pore pressure, P_p, is taken to be hydrostatic in the absence of other information. The friction coefficient, μ, ranges from 0.4 – 0.8 and in the absence of laboratory data is taken to be 0.6 (Moos and Zoback, 1990). Rock strength is assumed to be zero since fault planes already exist; the only resistance to slip is the frictional strength of the fault/fracture planes. Given a maximum or minimum stress and a reasonable value for friction, the minimum allowable value of σ_h or maximum value of σ_v can be determined using faulting theory. Typically, the overburden is known and using this method places a lower bound on σ_h.

2.1.2 Elasticity: Kirsch Equation to Find Stresses Around Wellbore

This method can be applied to analyze breakouts and drilling induced fractures to determine the ratio of maximum to minimum horizontal stresses required for the formation of each feature. The Kirsch equation (Kirsch, 1898) describes the effective tangential stress around a wellbore in terms of the minimum (σ_h) and maximum horizontal stresses (σ_H) shown in equation (2-3). Equations (2-4) and (2-5) show the simplified forms in terms of rock strength C and tensile strength T:

$$\sigma_{\theta\theta} = \sigma_{hmin}\left[\left(1+\frac{\sigma_{HMax}}{\sigma_{hmin}}\right)+\left(1-\frac{\sigma_{HMax}}{\sigma_{hmin}}\right)2\cos(2\theta)\right]-\alpha P_{pore}-P_{well\,bore} \quad (2-3)$$

$$\sigma_{\theta\theta Max} = 3\sigma_{HMax}-\sigma_{hmin}-\alpha P_{pore}-P_{well\,bore}\geq C \quad (2-4)$$

$$\sigma_{\theta\theta Min} = 3\sigma_{hmin}-\sigma_{HMax}-\alpha P_{pore}-P_{well\,bore} < -T \quad (2-5)$$

The angle θ is measured counter clockwise from the azimuth of the greatest principal stress (location of tensile fractures if any) as it appears in the wellbore. The overburden is assumed to be a principal stress whose axis is the wellbore. $P_{well\,bore}$ is the mud pressure in the wellbore which is assumed to be the same as pore pressure P_{pore} which would make the radial stress at the well bore wall zero. Values for α can be estimated through correlations or by looking at resistivity and sonic velocity data; low resistivity and high Vp/Vs ratios indicate a value closer to 1 while high resistivity and low Vp/Vs ratios indicate values closer to 0 (Moos and Barton, 1990). The tangential stress, $\sigma_{\theta\theta}$ is then compared to the uniaxial compressive strength, $C_{uniaxial}$, and the tensile strength,

T, to constrain the stresses. However, since at the borehole wall there are two stresses acting on the rock ($\sigma_{\theta\theta}$ and σ_v; σ_{zz} is assumed to be 0) the appropriate rock strength C to use is between the bi-axial strength (Wiebols and Cook, 1968; Moos and Zoback, 1990) C_b and the uniaxial strength C_o:

$$C_b = C_o\left(1 + 0.6\mu_f\right) \qquad (2-6)$$

$$C_o \leq C \leq C_o\left(1 + 0.6\mu_f\right) \qquad (2-7)$$

Where C_o=$C_{uniaxial}$ and μ_f is the coefficient of frictional sliding on microcracks. The inputs will be image log data (i.e. presence or lack of drilling induced fractures and breakouts), lab data for uniaxial strength and tensile strength, and well log correlations for these values. This method can also be applied in the absence of breakouts or tensile fractures. The Kirsch equation yields a range of valid stress values given the inputs. Combining this method with faulting theory serves to further constrain estimates.

2.1.3 Elasticity: Poisson's relation

Poisson's relation assumes that the main strain in rocks is associated with compaction due to the overburden. Horizontal strains are assumed to be negligible and the main source of horizontal stress is taken to be the horizontal deformation due to the overburden (Blanton et al., 1997):

$$\sigma_h = \frac{v}{1-v}\left(\sigma_v - \alpha P_p\right) + \alpha P_p \qquad (2-8)$$

This method approximates the minimum or average horizontal stress in quiescent basin settings. It must be applied cautiously, but regardless does provide a basic understanding of the horizontal stress state (Economides and Nolte, 1989). v is the Poisson's ratio, σ_v is the overburden, P_p is the pore pressure, and α is the Biot coefficient. Values for v and α can be correlated from sonic well logs and then calibrated with laboratory data if available. Values of σ_h should be checked to ensure they are within allowable ranges defined by faulting theory and the kirsch equation. Calibration with field data is usually necessary/helpful.

2.1.4 Elasticity: Lateral Strains and Temperature Effects

The previous equation (2-5) provides only a rough estimate of the minimum horizontal stress and requires calibration and guessing of the maximum horizontal stress. To improve on the estimate and provide an estimate of the maximum horizontal stress, horizontal strain terms are added in and stress due to temperature expansion (Blanton et al., 1997):

$$\sigma_h = \frac{v}{1-v}\left(\sigma_v - \alpha P_p\right) + \alpha P_p + [\varepsilon_h + v\varepsilon_H + (1-v)\alpha_t \Delta T]\frac{E}{1-v^2} \qquad (2-9)$$

$$\sigma_H = \frac{v}{1-v}\left(\sigma_v - \alpha P_p\right) + \alpha P_p + [\varepsilon_H + v\varepsilon_h + (1-v)\alpha_t \Delta T]\frac{E}{1-v^2} \qquad (2-10)$$

Poisson's ratio v, Overburden σ_v, Biot's coefficient α, and young's modulus E are correlated / calculated from well logs and calibrated with lab data where appropriate. The pore pressure P_p can be calculated as hydrostatic or taken from well logs. The coefficient of thermal expansion α_t is specific to the rock and usually on the order of 10^{-6}°F^{-1} (Blanton et al., 1997). The temperature change ΔT is the difference in the surface temperature and the temperature in the formation at a given point. The lateral strain additions ε_H and ε_h are manually changed until the estimated horizontal stresses satisfy conditions such as the limiting stress ratio in faulting theory, ranges defined by the Kirsch equation, data from a fracture test, fracture gradient data, dipole sonic data etc. However, since the strains in the equation model strains on a tectonic level and the geological history of units is quite complex, the values for the minimum and maximum horizontal strain may be negative to yield stress values that fit the data. From this perspective they should be viewed as fit parameters rather than actual strains. Ideally, all the above methods are applied when estimating stresses.

2.2 Determining Stress Orientations

The orientations of the principal stresses are determined from earthquake fault plane solutions, wellbore breakout analysis (Bell, J.S. and Gough, D.I. (1979), Amdei, 19997) via image logs, caliper logs, sonic logs etc. Other geologic data such as mineral growth patterns can provide additional evidence (Zoback, 2010). Assuming stress orientations are the regional orientations determined from earthquake patterns is a simplifying assumption in the absence of other data. However, image logs are relatively common and determining the presence and orientations of breakouts and drilling induced fractures is a simple task. σ_H is taken to be at the azimuth of the drilling induced fractures and σ_h is taken to be the azimuth of the breakouts.

2.3 Workflow

2.3.1 Data and Model Preparation

Prior to commencing the modeling effort, the available data must be checked for quality and to ensure there are no key data missing. A common example of missing data is laboratory data used to calibrate well logs and correlations. Lab tests are expensive and may be neglected as cost cutting measures. However, many correlations in particular rock strength correlations are empirical making it difficult to replace field specific lab tests with more generic rock type data available elsewhere. Fortunately, part of this study involves acquiring laboratory measurements which will be used in the correlations. A coordinate system must be selected for the model, typically a projected coordinate system since many of the outputs of the MEM will be used as inputs to other modeling software and keeping units in length instead of degrees aids this process.

2.3.2 Building 1-D MEMs

This step involves calculating, correlating, and calibrating needed data along the wellbores. Well log data that is available such as density, sonic, and porosity logs must be quality controlled using caliper logs to ensure spurious data points are removed. There are three possible rock type scenarios: isotropic, transversely isotropic, and orthotropic. The isotropic case applies best for the model constructed herein (i.e. the properties calculation methods are the same in all directions). Isotropy in this case applies to the rock types within the reservoir. The properties themeselves vary (sometimes significantly). The sonic data gathered from well logs is used to calculate the elements of the stiffness matrix in the isotropic case (Frydman, 2010):

$$\begin{bmatrix} \sigma_x \\ \sigma_y \\ \sigma_z \\ \tau_{xz} \\ \tau_{yz} \\ \tau_{xy} \end{bmatrix} = \begin{bmatrix} C_{11} & C_{12} & C_{12} & 0 & 0 & 0 \\ C_{12} & C_{11} & C_{12} & 0 & 0 & 0 \\ C_{12} & C_{12} & C_{11} & 0 & 0 & 0 \\ 0 & 0 & 0 & C_{66} & 0 & 0 \\ 0 & 0 & 0 & 0 & C_{66} & 0 \\ 0 & 0 & 0 & 0 & 0 & C_{66} \end{bmatrix} \begin{bmatrix} \varepsilon_x \\ \varepsilon_y \\ \varepsilon_z \\ \gamma_{xz} \\ \gamma_{yz} \\ \gamma_{xy} \end{bmatrix} \qquad (2-11)$$

$$C_{12} = C_{11} - 2C_{66} \qquad (2-12)$$

In this scenario there are only 3 separate terms that require calculation all of which can be determined from the vertical Vp and Vs (Frydman, 2010):

$$C_{11} = \rho V_p^2 \qquad (2-13)$$

$$C_{66} = \rho V_s^2 \qquad (2-14)$$

$$C_{12} = \rho\left(V_p^2 - 2V_s^2\right) \qquad (2-15)$$

Inverting the matrix (equation 2-11) gives:

$$\begin{bmatrix} \varepsilon_x \\ \varepsilon_y \\ \varepsilon_z \\ \gamma_{xz} \\ \gamma_{yz} \\ \gamma_{xy} \end{bmatrix} = \begin{bmatrix} 1/_E & -v/_E & -v/_E & 0 & 0 & 0 \\ -v/_E & 1/_E & -v/_E & 0 & 0 & 0 \\ -v/_E & -v/_E & 1/_E & 0 & 0 & 0 \\ 0 & 0 & 0 & \mu & 0 & 0 \\ 0 & 0 & 0 & 0 & \mu & 0 \\ 0 & 0 & 0 & 0 & 0 & \mu \end{bmatrix} \begin{bmatrix} \sigma_x \\ \sigma_y \\ \sigma_z \\ \tau_{xz} \\ \tau_{yz} \\ \tau_{xy} \end{bmatrix} \qquad (2-16)$$

The matrix can now be solved in terms of Vp, Vs, and density to yield equations for Poisson's ratio, young's modulus, and the shear modulus along the entirety of the log:

$$v = \frac{\left({}^{v_p}/_{v_s}\right)^2 - 2}{2[\left({}^{v_p}/_{v_s}\right)^2 - 1]} \qquad (2-17)$$

$$E = \rho v_s^2 \frac{3\left({}^{v_p}/_{v_s}\right)^2 - 4}{\left({}^{v_p}/_{v_s}\right)^2 - 1} \qquad (2-18)$$

$$\mu = \rho v_s^2 \qquad (2-19)$$

The density used in the above equations ρ is taken from the density log. The mechanical parameters will then be defined at the resolution of the well log along the length of the well bore. In many older well log data suites, shear velocity data was not gathered. If this is the case, simple curve fitting relationships such as that shown in Figure 11 are used to estimate the Vp/Vs ratio. Overburden σ_v is calculated by integrating the density log:

$$\sigma_v = \int_0^z \rho(z) g dz \approx \bar{\rho} g z \qquad (2-20)$$

The function $\rho(z)$ is a function of the densities along the well bore. A density log typically is used for this term. g is the acceleration due to gravity and z is the height increment. Pore pressure is similarly calculated in the absence of pressure logs or other measurements:

$$P_p^{hydro} = \int_0^z \rho_w(z) g dz \approx \bar{\rho}_w g z_w \qquad (2-21)$$

Pressure is taken to be hydrostatic pressure P_p^{hydro} at a given depth z from the top of the water table. Factors affecting this value are salinity of fluid and possible over pressure in the formations drilled. Key parameters requiring correlation are Unconfined Compressive Strength (UCS) and Ultimate Tensile Strength (UTS). Additional correlations must be applied to obtain estimations for values of static Young's modulus and Poisson's ratio since they will most likely be different and more applicable to the problem of reservoir characterization (King, 1983; Ide, 1936; Eissa and Kazi, 1988). These correlations are always empirical and created for a specific field though some can be used for a similar rock type such as correlations developed for sandstone and limestone. Correlations for mechanical parameters in sedimentary rocks have been proposed by Najibi et al. (2015), Wang (2000), Oyler et al. (2010) and Plumb et al. (2000) while Lai et al. (2014) developed a correlation for UCS in Malaysian granite.

2.3.3 Lithological Grouping

A key decision is made at this stage of the modeling process: how much stratigraphic detail is it appropriate to include? The validity of the model generated depends heavily on correctly grouping zones of similar properties so that the apparent heterogeneity in the model as closely as possible describes the actual heterogeneity of the formation modeled. Grouping for example a primarily sandstone unit with a primarily limestone unit will result in a 3-D model that is essentially a hybrid of the two units. Spence et al. (2014) describes the importance of properly grouping units with the concept of mechanical stratigraphy. Mechanical stratigraphy means distinguishing units based on observed changes in fracture data and properties such as porosity, density, gamma ray response, and resistivity to delineate zones of different mechanical behaviors. Frequently, the mechanical stratigraphy coincides with the rock type boundaries, however, the possibility exists for sizeable changes within a rock unit. Examples of this may be different volcanism episodes causing compositional and crystal size changes in granites that are juxtaposed or a sandstone layer that has some shaley sections.

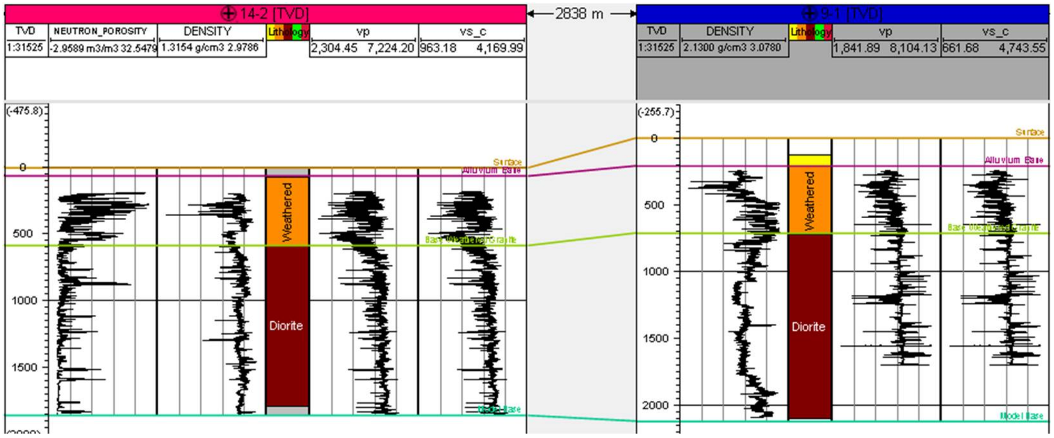

Figure 4: Correlations of chosen units across wells; geology correlates well with mechanical stratigraphy in this case

Once the mechanical stratigraphic breaks have been chosen on each well, they are correlated (Figure 4) and used to create structural surfaces.

2.3.4 Building the Structural/Geologic Model

To create a structural model, layers defining the mechanical stratigraphy from the previous step are combined with fault picks to create offset units if necessary. Determining the presence of faults and their orientations is easy in well-defined areas with 3-D seismic surveys available, however, geothermal projects are frequently lower budget and 3-D data sets are not always available. In cases such as these, conducting a thorough literature review may be necessary to determine the structural consensus. Gravity data can also be used if necessary to support possible structures or to develop new structural models since gravity data is readily available and easy to work with. Faults can be interpreted directly from seismic, drawn onto cross sections, or drawn freehand. Once the number, location, and attributes of the faults have been selected, they are gridded into the mechanical stratigraphy picks (Figure 5).

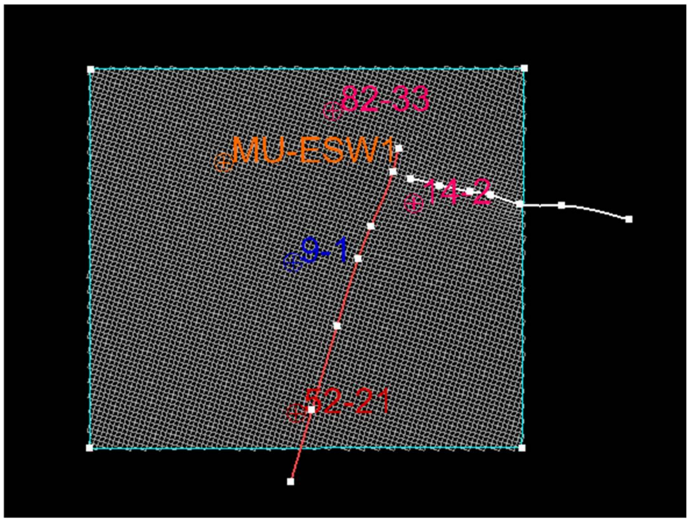

Figure 5:Model boundary with well locations and faults shown gridded into the model

The grid cell dimensions should be about the size of the smallest feature the model is intended to capture computational power allowing. The vertical dimensions are chosen using a layering scheme which will depend on the depositional environment and current orientations of the units being modeled (Yarus and Chambers, 2006).

2.3.5 Property Modeling

Facies modeling is useful in reservoirs with a high degree of heterogeneity, however, geothermal reservoirs are typically in granite which is relatively homogenous. Facies models are created using geostatistical algorithms such as Sequential Indicator Simulation which probabilistically estimate the rock type at each grid cell location given as inputs well log lithology data and previously modeled cells. These algorithms use variograms to model large scale trends, caused by an ocean current during deposition for example, and structures. Variograms accomplish this by allowing the user to set limits on how far in each of the three axes the data seem to be correlated on a certain scale; these limits are called ranges (Gringarten and Deutsch, 2001).

The 1-D MEMs previously generated are then interpolated throughout the 3-D structural model using stochastic algorithms such as sequential gaussian simulation or deterministic algorithms such as Krigging where necessary. Stochastic algorithms are useful for determining the variabilities in UCS, UTS, porosity, and density within units. However, because of the random nature of the models generated they are not suitable for modeling stress direction changes between wells for example. In situations such as these, Krigging is used to obtain the best fit model of the data. The modeled 3-D property volumes should be compared to the input data to ensure the simulated distributions are similar to the input distributions.

2.3.6 In-situ Stress Modeling from 1D MEMs and Direction Determination

The stress magnitudes and directions are estimated using the methods outlined in sections 2.2 and 2.3 above. The inputs for pore pressure, UTS, and UCS are taken from the 1-D MEM's generated using correlations. Magnitude data for the principal stresses once estimated can be interpolated independently or in tensor form including directional data. If data from more than one well is available, and there is significant direction change, the stress tensors can be rotated to a common geographic frame of reference and the individual parts of the tensor can be interpolated using the Krigging algorithm and subsequently re-constructed and plotted. This reveals a type of vector flow diagram demonstrating stress direction changes on a small scale. This type of modeling will not be done in this work.

2.3.7 Modeling In-situ Fractures

An important final step in building a MEM is modeling the in-situ fracture networks. In-situ fracture networks play a large role in how the reservoir will respond to stimulation since permeability will be increased largely via shearing of pre-existing fractures and the propagation of these fractures (Kamali and Ghassemi, 2017). Since the host rock of geothermal reservoirs is typically granite with high UCS and UTS (Wang et al., 2016; Bakshi et al., 2016), the stimulation efforts will likely be hijacked by the fracture network since the sealing material will have much lower UTS. Discrete fracture data sources are seismic surveys, borehole image logs, 4-arm caliper logs, and outcrop data. Some or all of these sources may be available. These data are compiled and analyzed to determine the correct length and aperture models best fit the individual fracture sets. Fractures along the borehole are summarized by various intensity attributes, however, the P32 value is commonly calculated and will be used herein. The P32 log is defined as the average surface area of the two sides of a fracture per volume of rock. This property is estimated along the wellbore by calculating the surface area of intersecting fractures. This is accomplished by assuming the fracture traces along the well bore represent an intersecting plane. Assuming this, the area of the intersecting plane can be calculated. This attribute can then be interpolated across the 3-D volume to provide guidance to the software when placing fractures. Deterministic or stochastic algorithms can be used to create DFN models. Often there is not enough data to generate deterministic models, while stochastic models can be generated based on outcrops and educated guesses. The DFN generated in this thesis will apply stochastic methods.

Chapter 3 Building the Mechanical Model

3.1 Data and Model Preparation

Data available for this site constitute well logs, geophysical surveys, geological maps, and past geological interpretations. Well logs available and used in this modeling effort are listed in Table 1.

3.1.1 Well Log Data

Of the six wells near the FORGE site, only data from 52-21, 9-1,14-2, and MU-ESW1 will be used. Acord 1-26 is >10 km from the FORGE site and would require a modeling area several kilometers larger introducing more uncertainty due to the extra area without data coverage. The full suite of log data available for MU-ESW1 far exceeds the logs listed in Table 1, however, only the logs used in this project are listed. The data in 82-33 is also excluded from the modeling process because the sonic slowness log exhibits very erratic behavior probably because of heavy fracturing. 82-33 is drilled near the closest points of the Negro Mag and Opal Mound faults so it is possible that differential motion along these features caused areas of intense fracturing. Since key parameters such as Young's Modulus, Poisson's ratio, and UCS are calculated/correlated from the sonic data, it is important that the data indicate reasonable average values with minimal spikes.

Table 1: Available Used Well Log Data

Logs	1-26	52-21	9-1	14-2	82-33	MU-ESW1
Gamma	x	x	x	x	x	x
Density	x	x	x	x	x	x
Neutron Phi	x	x		x	x	x
Sonic	x	x	x	x	x	x
Lithology	x	x	x	x	x	x
Caliper	x	x	x	x	x	x

3.1.2 Geophysical Surveys

The most prominent 3-D geophysical data available is a comprehensive set of gravity data and an associated 3-D model (Hardwick et al., 2016). Three seismic interpretations are available near the Acord 1-26 well (Shannon et al., 1983) and 1 large scale (>100 km) interpretation by Smith and Bruhn (1984) cuts across the western half of Southern Utah through the Mineral Mountains and into Nevada. A fifth 2-D seismic line (yellow arrow in Figure 7) which crosses the Opal Mound fault near Well 9-1 (Ross et al., 1982) was reprocessed and re-interpreted as part of the FORGE project. Unfortunately, the interpretations near Acord 1-26 showing large fault offsets are inconsistent with the re-processed data and Bruhn and Smith's (1984) findings. The locations of the seismic lines in Milford valley and relative to the model area are shown in Figure 6. The later show a continuous sloping basement with offsets eroded away through uplift of the Mineral Mountains. The 2-D line near the FORGE site combined with the gravity interpretation are heavily relied on to provide guidance in designing and creating the structure. Magneto Telluric and Resistivity data sets (Wannamaker et al., 1978; Ward and Crebs, 1975) are also available but of little use to the modeling effort outlined herein due to their coarseness.

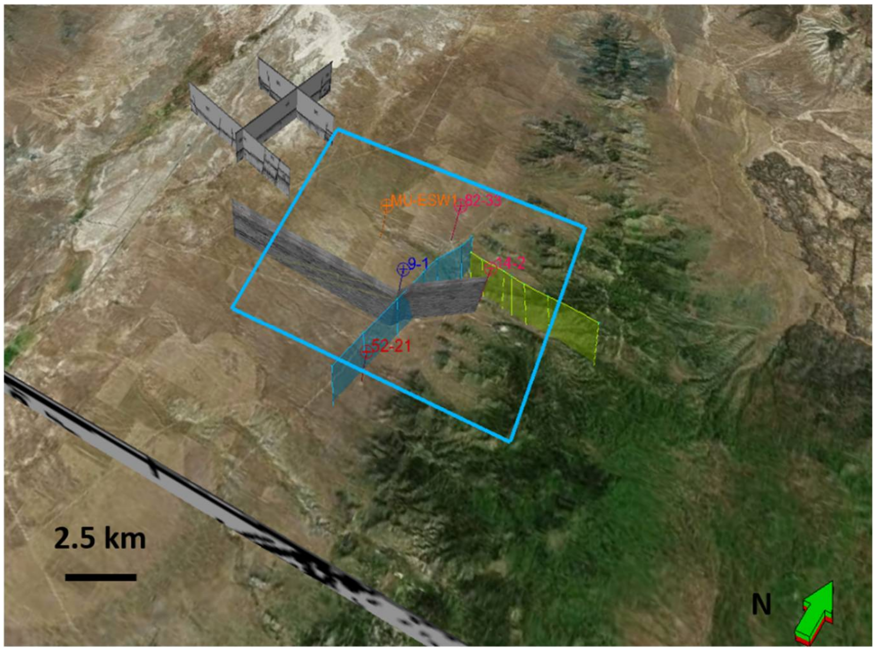

Figure 6: Locations of 2D seismic lines with respect to wells and modeling boundary (blue boundary); Opal Mound fault is shown in blue and the Negro Mag fault is shown in yellow (Bing maps, May, 2018)

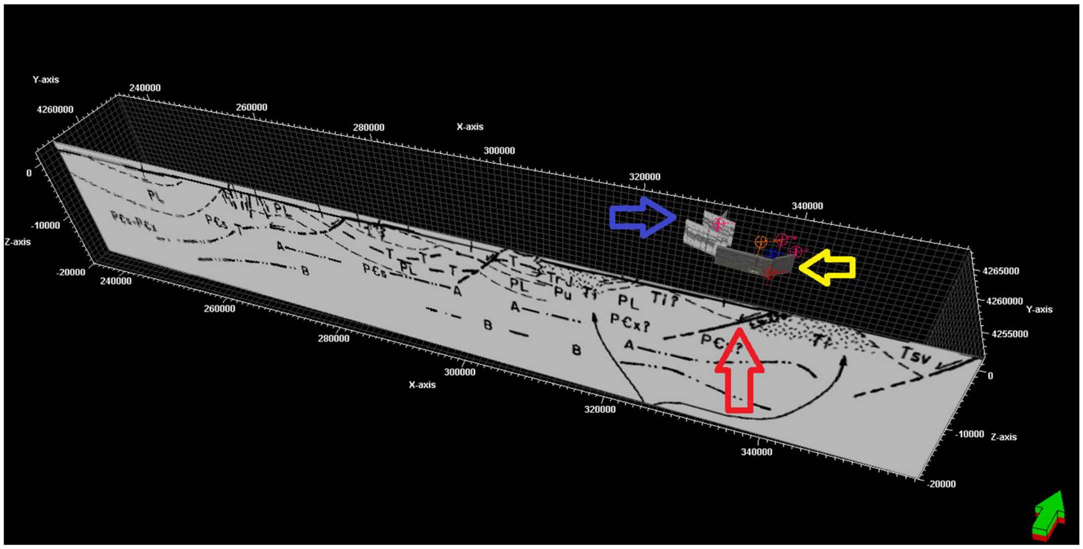

Figure 7: Relative locations of five 2D seismic lines available. Red arrow on large line provided by Bruhn (1984) shows the location of Milford valley. The yellow arrow shows the seismic line in Ross et al. (1982) which crosses the Opal Mound fault and provides the most useful information for the FORGE site. The blue arrow points out the location of the three 2D seismic lines around well Acord 1-26

3.1.3 Geological Data

Geological data available for the site are geological maps (or other surface interpretations), structural interpretations, conceptual models, mud logging data from wells, and mineralogical descriptions of the different intrusive phases.

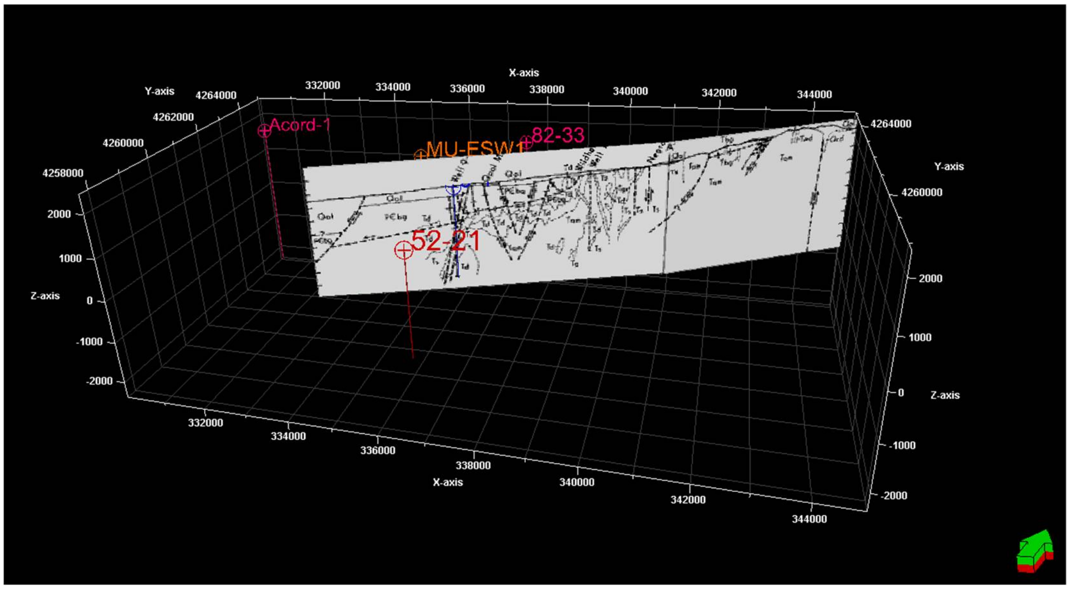

Figure 8: Cross section of the Mineral Mountains and Milford valley area (Nielson, 1986) shown in 3D

Faulder (1991) outlined the KGRA (known geothermal resource area) at the Roosevelt Hot Springs describing the key structures (opal mound fault and negro mag fault), fracture and joint patterns, and the main intrusive groups. Shannon et al. (1983) describes in detail the units penetrated by Acord 1-26 giving detailed descriptions of the alluvium. Nielson et al., (1986) provided some of the most detailed mapping efforts and structural interpretations (until recently) of the Mineral Mountains. This work integrated geological mapping efforts and well data with conventional wisdom of basin-range structures to produce several cross-sections (Figures 8 and 9) showing relationships between listric fault structures (e.g. Wildhorse Canyon Fault) and high angle faults (e.g. Opal Mound fault). Simmons et al. (2016) compile past analyses to generate rock type descriptions/correlations for Acord 1-26, 9-1, 52-21, and 14-2. This manuscript also includes brief analyses of outcrop fractures. Evans and Nash (1978) describe in detail the quaternary rhyolites in the Mineral Mountains.

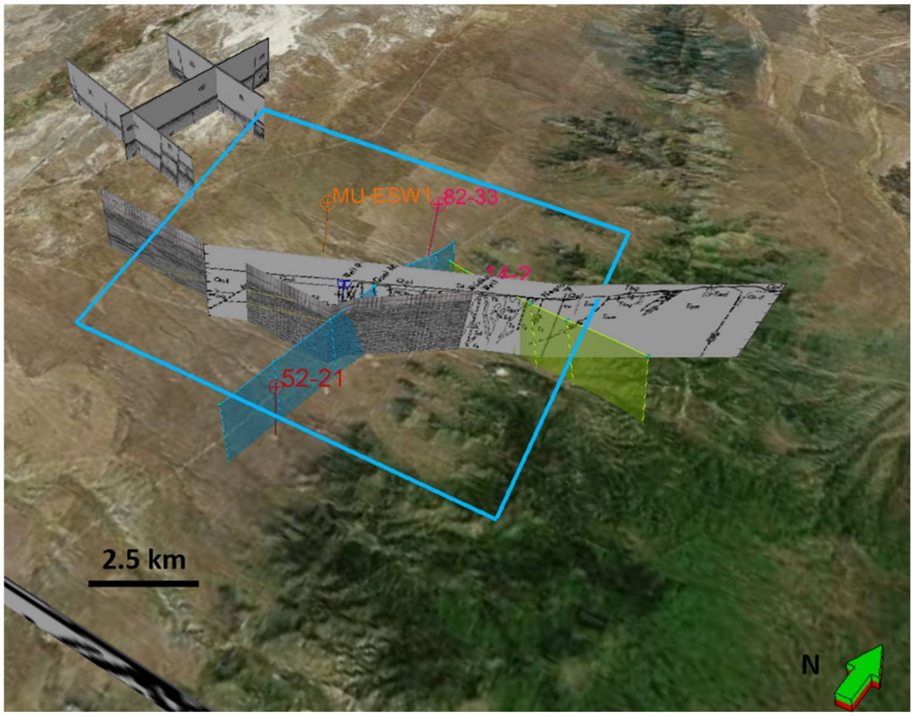

Figure 9: Location of cross section (Nielson, 1986) displayed with model extent, faults, seismic lines and well data (Bing maps, May, 2018)

3.1.4 Laboratory Data

Laboratory data is available for the granodiorite and granite at reservoir depths. Lithology 1 is a pink large crystalled rock from around 6800 ft depth in well MU-ESW1 and lithology 2 is a fine grained dark colored crystalline rock with a distinctive fabric from around 7500 ft depth.

Table 2: Rock mechanical parameters (EGI, 2018)

Lithology	1	1	2	2
Orientation	Vertical	Horizontal	Vertical	Horizontal
Friction Angle (degrees)	51.3	43.5	52.8	53.5
Poisson’s Ratio	0.2174	0.2078	N/A	N/A
Density (g/cc)	2.64	2.64	N/A	N/A
Porosity (%)	0.46	0.46	N/A	N/A
UCS (MPa)	121	104.54	N/A	N/A
Young’ Modulus at (GPa)	45.9	54.95	N/A	N/A

The average properties for both lithologies are relatively similar with the notable exception of the friction angle for lithology 1. These properties will be used to calibrate UCS, Young’s modulus, and Poisson’s ratio correlated from well logs. The average friction angle, 50.27, will be used to estimate friction in stress analysis.

3.2 Building 1-D MEMs

The new well drilled in the FORGE site MU-ESW1 is 7574 ft deep and a complete suite of logs were run in it. Sonic and density logs from the other five deep wells (Table 1) were digitized and assessed for quality; two of the wells are left out of the modeling effort, Acord 1-26 and 82-33. Since no shear sonic logs are available in the other wells, the shear velocity and compressional velocity logs from MU-ESW1 will be used to develop correlations which can be applied to the other three wells to estimate needed properties.

3.2.1 Correlations

Poisson's ratio and Young's modulus were calculated from the shear and compressional sonic data in MU-ESW1 using equations 2-17 and 2-18. The UCS in MPa was calculated using the correlation presented by Lai et al. (2014) developed in Malaysian:

$$UCS\ (MPa) = 0.0000255 \Delta T^{1.7658} \qquad (3-1)$$

The compressional sonic speed ΔT is in meters per second. The correlated values of rock uniaxial strength are calibrated with the lab data in Table 2. Tensile strength is assumed to be about 10% of the UCS. Overburden is integrated from the density logs using equation 2-20.

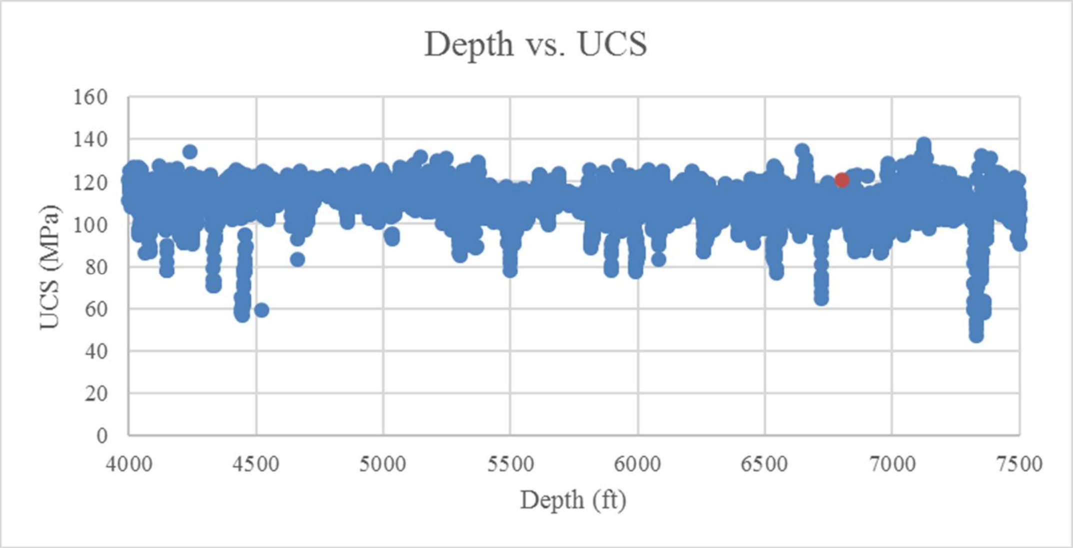

Figure 10: Blue points are vertical UCS values correlated using Lai et al. (2014); the red point is laboratory data. The values are close and do not require shifting

Since the three other deep wells used do not have shear velocity logs, a cross plot and fit curve (Figure 9) were developed to estimate these values where absent. The relation used was:

$$Vs\left(\frac{m}{s}\right) = 0.651822 * Vp\left(\frac{m}{s}\right) - 538.905 \qquad (3-2)$$

The fit coefficient was 0.921. This relationship was used to estimate shear velocity values in wells 52-21, 9-1, and 14-2.

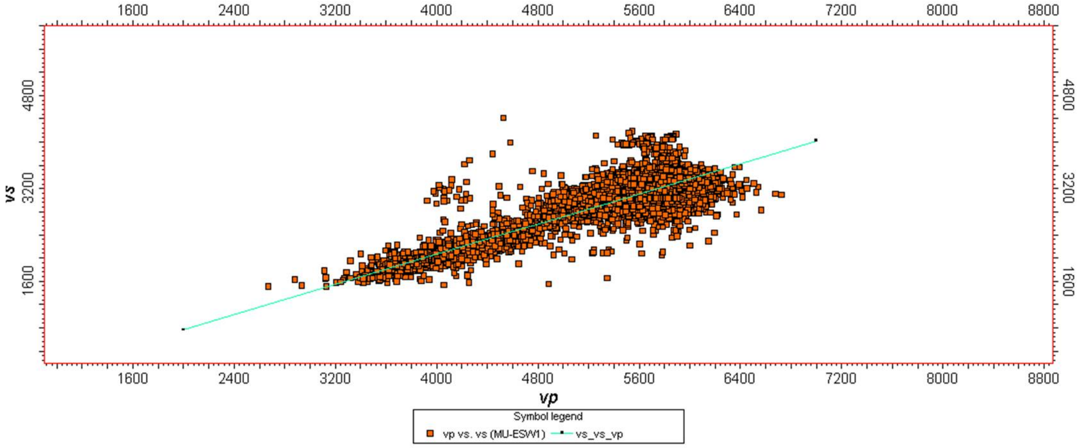

Figure 11: Correlation of Vp vs. Vs (meters/second) in well MU-ESW1

Once values of Vs were estimated, they were then used to calculated dynamic values for Poisson’s ratio and Young’s modulus. However, for our applications, static values for these parameters are preferable since they represent the response to larger loads applied over extended periods of time. Eissa and Kazi (1988) conducted a thorough study of the correlation between the dynamic and static Young’s modulus using 342 data points from literature. Their correlation was developed using a variety of rocks.

$$log_{10}(E_{st}) = 0.02 - 0.77 log_{10}(\rho E_{dyn}) \quad (3-3)$$

The logarithm of E_{st} (static modulus) can be linearly correlated to the logarithm of ρE_{dyn} (density times dynamic modulus) where ρ is in g/cc and values of the modulus are in GPa. This correlation is applied to estimate the static moduli (Figure 12). Note the static values in granite (reservoir rocks) below about 3500 ft are significantly smaller.

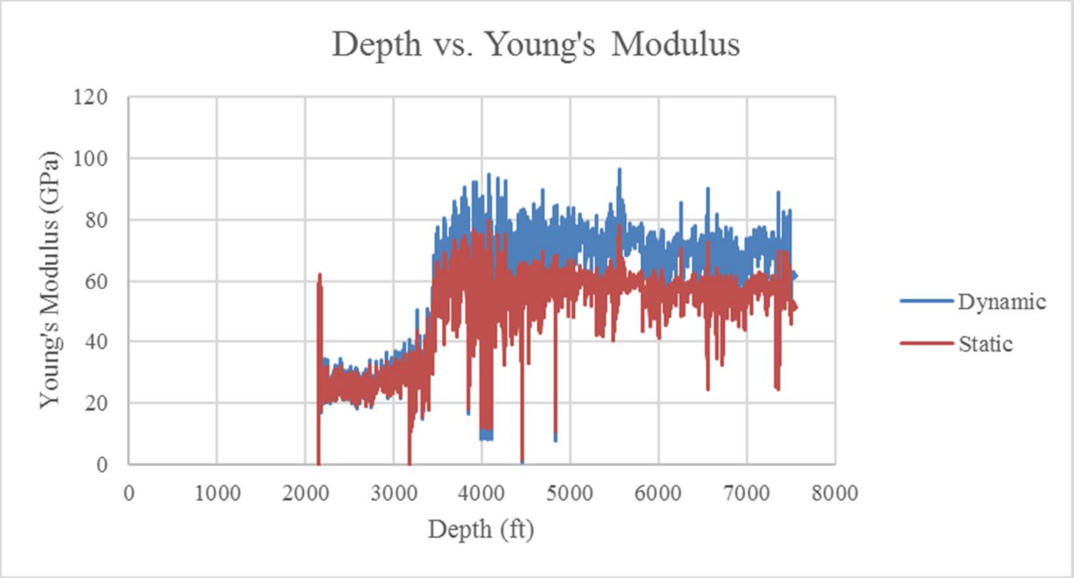

Figure 12: Static and dynamic values of Young's modulus in well MU-ESW1; dynamic values are calculated from sonic and density logs and static values are correlated applying Eissa and Kazi (1988). Variations in values in the upper few thousand feet are due to differing rock types

Correlations are also needed to estimate static values of Poisson’s ratio. A shift is applied to the average of our values using the average value for granite in the site (Table 2) of about 0.205. For example, average dynamic values of Poisson’s ratio in MU-ESW1 are about .278; applying the shift (.278-.205=0.073) 0.073 was subtracted from every value. This shift was applied to all wells in the field to bring their average dynamic Poisson's ratio values in line with static values.

The effects of temperature on the mechanical properties of granite must also be considered in geothermal applications. Takarli and Prince-Agbodjan (2008) explored this topic experimentally and determined that sonic compressional velocities do not change at a significant rate until temperatures above 500 C have been achieved (Figure 13). Similarly, the elasticity of the samples they tested did not exhibit significant changes below 500 C (Figure 14).

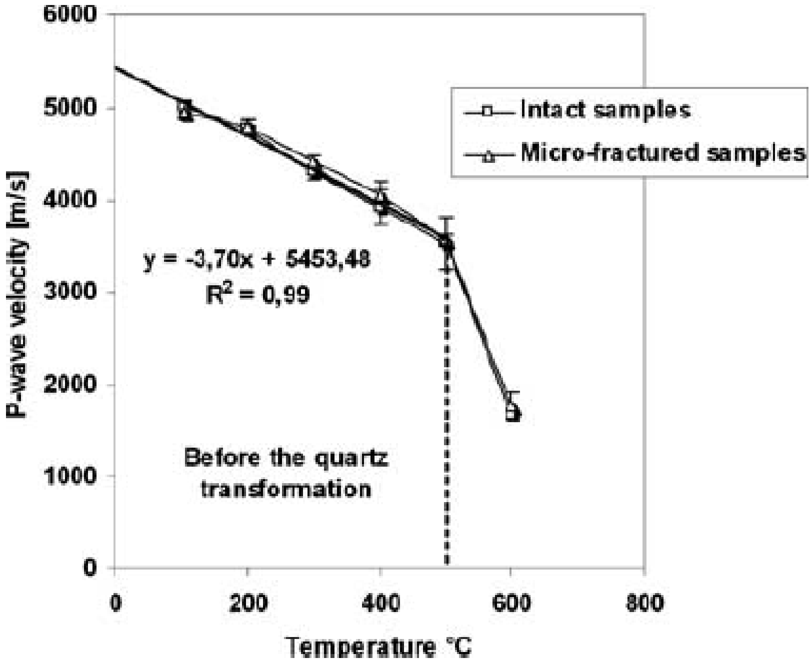

Figure 13: Variation in P-wave velocities with temperature in granite (Takarli and Prince-Agbodjan, 2008). At temperatures present at the FORGE site at reservoir depths, P-wave velocity should not vary much though some change will be present.

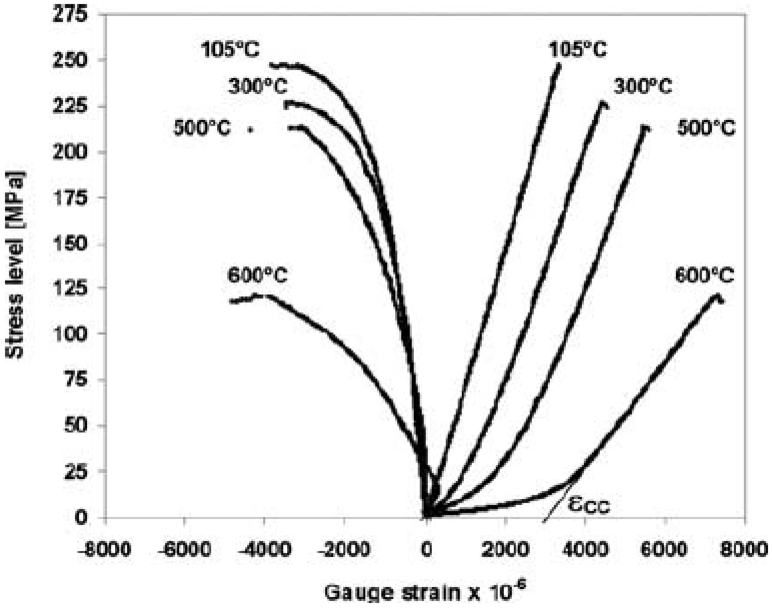

Figure 14: Stress strain curves for heated granite. Not the slopes of the curves above 500 C do not change much above 25 MPa differential stress. Figure taken from Takarli and Prince-Agbodjan (2008).

Since temperatures in excess just under 150 C exist in MU-ESW1, effects undoubtedly exist but they are minimal. The well log data should also accommodate some of this since the rock sampled by the logging tools is elevated in temperature somewhat. Given these, the effects of temperature are neglected in property calculation along the well bore.

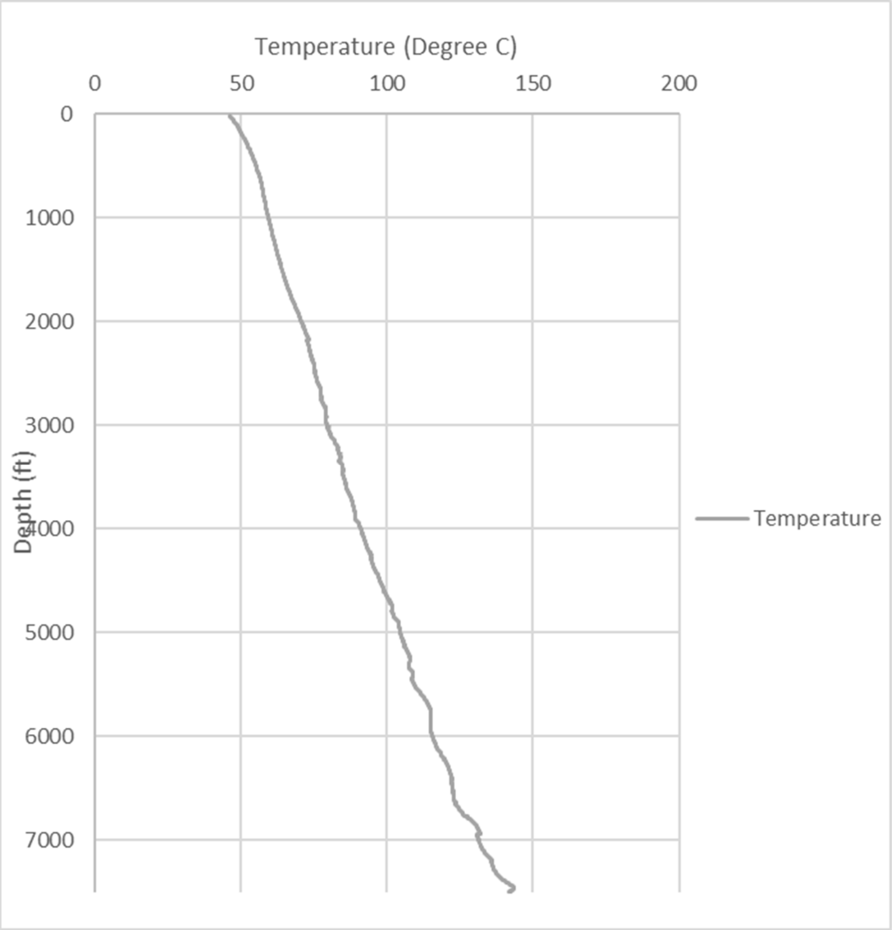

Figure 15: Temperature in well MU-ESW1 with depth taken from well logs. Temperature does not exceed 150 C

3.2.2 Stress Estimates

Stress magnitudes prove difficult to estimate without field data. Fortunately, in-situ stresses have been measured through injection tests (EGI, 2018). Two important factors must be considered: 1.) Pore pressure at the FORGE site 2.) Stress due to temperature. Measurements taken in the deep wells indicate hydrostatic pore pressure (EGI, 2018) and image logs from MU-ESW1 and sonic logs in 82-33 (Figure 16) show the reservoir rocks are heavily fractured.

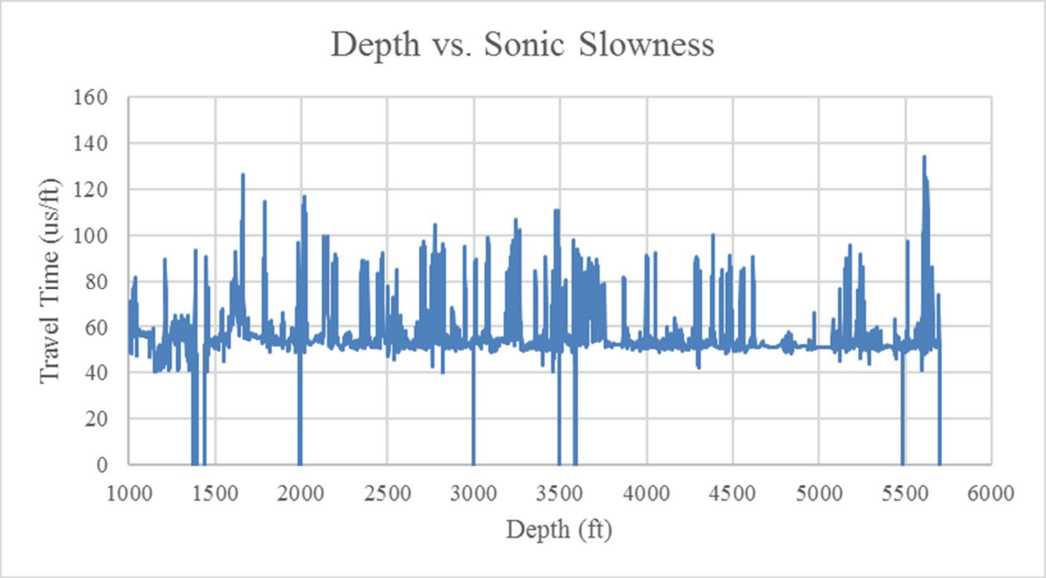

Figure 16: 82-33 Compressional sonic slowness log. The spikes in travel time are interpreted to indicate heavy fracturing.

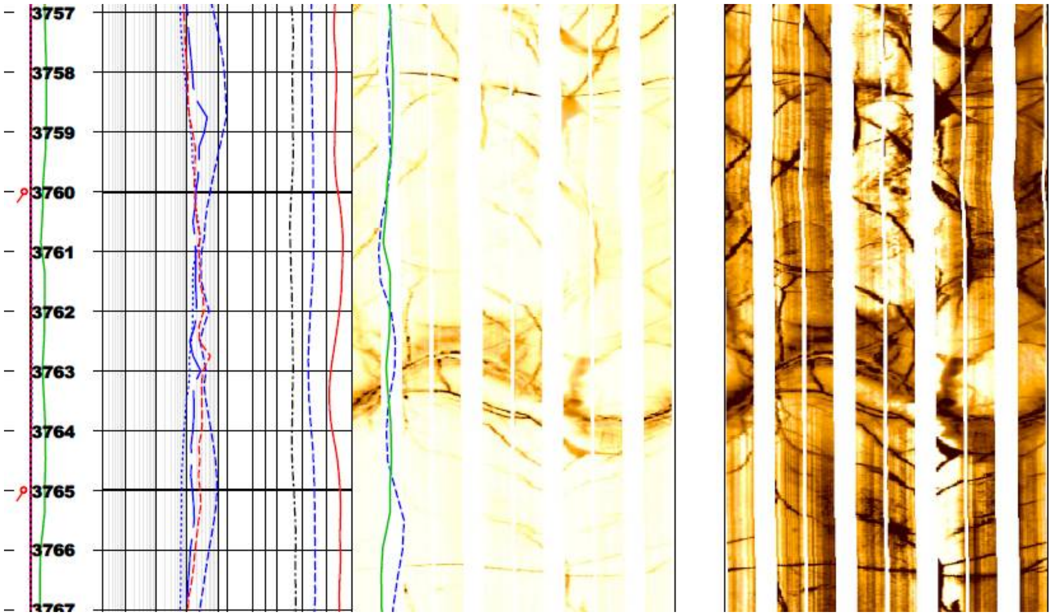

Figure 17: Section of image log in MU-ESW1 indicating heavily fractured rock

Given these, we will assume hydrostatic pore pressure. The horizontal stress due to thermal expansion must be addressed since temperatures in excess of 250 C are present near the Opal Mound fault. The maximum possible horizontal thermal stress between two points is given by (Nielson, 1989):

$$\sigma_{therm} = \frac{\alpha_t \Delta T E}{1 - v} \qquad (3-4)$$

Nielson (1989) uses 10^-5 K^-1 for α_t, v is about .205 (Table 2), and E is about 50 GPa (Table 2). ΔT is the difference in temperature between the two points. MU-ESW1 well is 180-190 C at 6800 ft. Wells 52-21 and 82-33 predict similar temperatures at these depths (Allis et al., 2016)). Well 9-1, however, is about 225 C at reservoir depths. Thus for 82-33 and 52-21 ΔT is about 10 C and about 45 C for 9-1. The FORGE site is about 2.5 km from wells 82-33 and 9-1 and 5.5 km from 52-21.

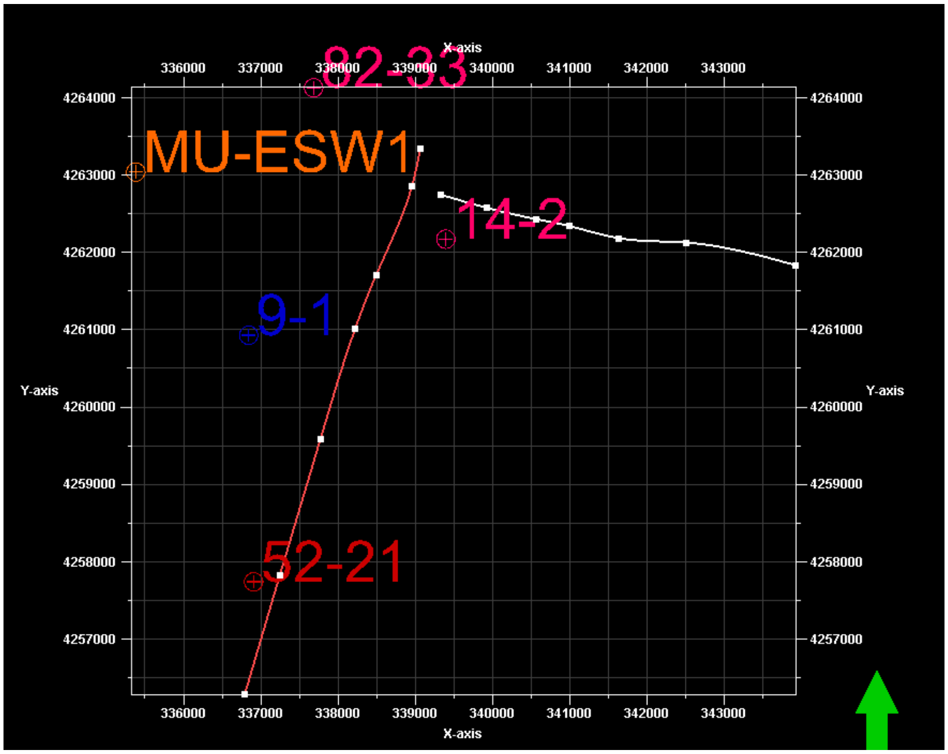

Figure 18: Spatial relationships between FORGE wells, Opal Mound fault and Negro Mag fault. The red line is the Opal Mound fault and the white line is the Negro Mag fault.

Using these values, the maximum thermal stress between the MU-ESW1 well and 82-33 is about 6.3 MPa or about 0.003 MPa/m. The maximum thermal stress between MU-ESW1 and 9-1 is 28.3 MPa or about 0.011 MPa/m. The gradient between MU-ESW1 and 9-1 is equivalent to about .423 psi/ft or roughly the same as a hydrostatic pressure gradient so it is not insignificant. However, these are maximum possible values and the actual values are likely significantly lower. The temperature anomaly has been present through several episodes of faulting. Additionally, there is significant seismicity within the hot springs and recent activity on the opal mound fault

(Nielson, 1989). These structures likely have provided relief for thermal stresses. Therefore, in-situ stress estimates in this work will not include thermal effects.

The FORGE site is in a normal faulting stress regime though the Negro Mag fault seems to indicate a large strike slip component. The thermal stress closer to the Opal Mound fault and Negro mag fault are significantly higher or have been higher in the past due to the higher temperature gradient and possibly contribute to the abnormal fault structures within the RHS site.

First, faulting theory is applied to generate the limiting stress ratio and the minimum possible horizontal stress given the overburden generated from well logs using a friction angle of 50.27° which is the average value in Table 2 above and μ of about 1.202:

$$Limiting\ Ratio = \left(\left(1+\mu^2\right)^{\frac{1}{2}} + \mu\right)^2 \approx 7.649 \qquad (3-5)$$

Using this value, the ratio can be applied:

$$\frac{\sigma_v - P_p}{\sigma_h - P_p} < 7.649 \qquad (3-6)$$

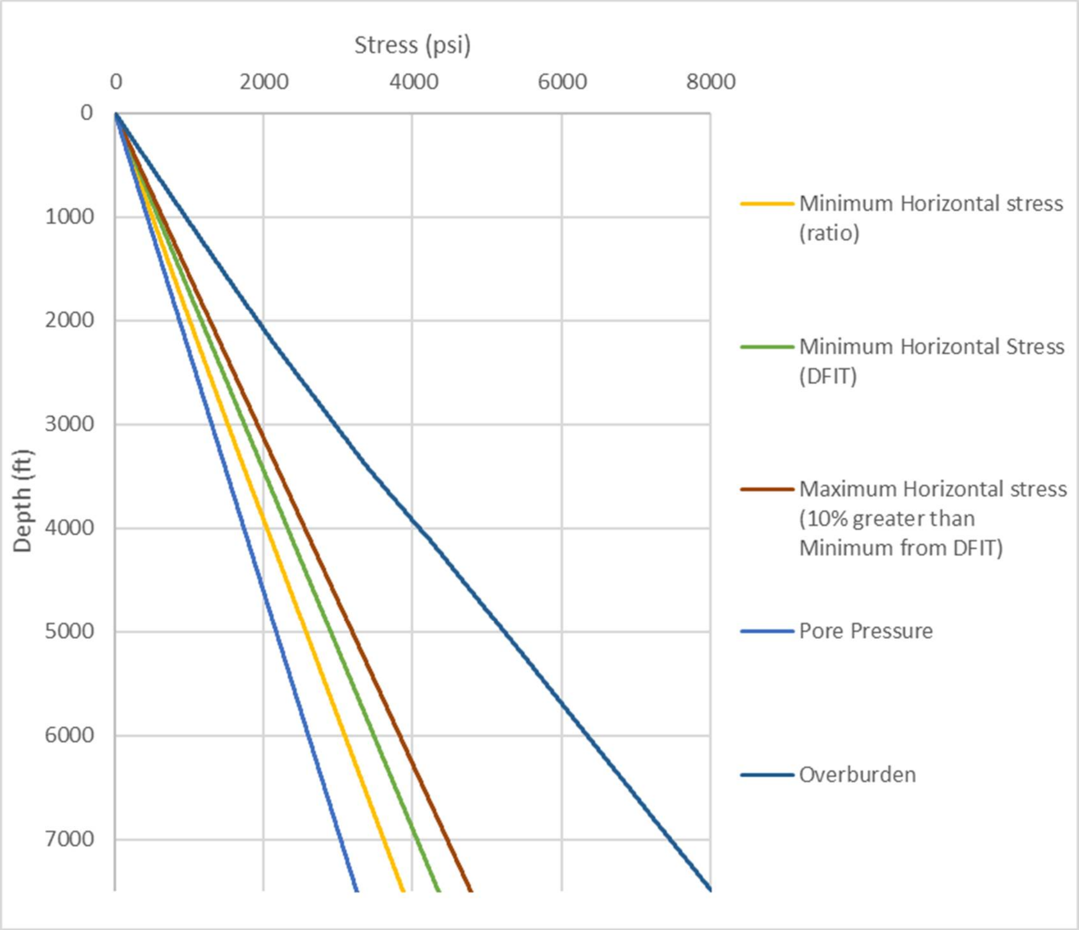

Figure 19: From left to right: pore pressure, limiting stress, minimum horizontal stress from injection test, max horizontal stress from injection test, and overburden

This applies a lower bound to our minimum horizontal stress estimations. Figure 19 above shows the relationship between pore pressure, the limiting stress ratio, the horizontal stresses estimated from the injection test and the overburden. Next, in order to model small scale variations in horizontal stress we apply elasticity theory using the strain corrected estimation for basins in which the primary cause of horizontal stress is pore pressure and the Poisson effect (i.e. low horizontal stresses) (Blanton et al., 1997):

$$\sigma_h = \frac{v_{st}}{1 - v_{st}}\left(\sigma_v - \alpha P_p\right) + \alpha P_p + [\varepsilon_h + v_{st}\varepsilon_H]\frac{E_{st}}{1 - v_{st}^2} \qquad (3-7)$$

$$\sigma_H = \frac{v_{st}}{1 - v_{st}}\left(\sigma_v - \alpha P_p\right) + \alpha P_p + [\varepsilon_H + v_{st}\varepsilon_h]\frac{E_{st}}{1 - v_{st}^2} \qquad (3-8)$$

The effects of temperature are excluded as previously discussed. Values of Poisson's ratio and Young's modulus used are static. The key usefulness of this method is that it provides an estimate of the maximum horizontal stress at each point along the wellbore where dynamic data is available. Data from the injection test completed in the interval between 7374.9 ft and 7500 ft depth in MU-ESW1 indicate a minimum horizontal stress of about 4275 psi and a maximum stress about 10% greater (EGI, 2018). The minimum horizontal stress gradient is estimated to be about 0.62 psi/ft. The stress values estimated on the wellbores are averaged along the massive granite in the lower portion to exclude any weathered material. The injection test revealed minimum horizontal stresses about 275 psi greater than the minimum possible stress indicated by the limiting ratio. The above constraints are applied to the averages of the dynamic values along the wellbore by varying the strain coefficients (ε_h and ε_H) until the average maximum stress is about 10% greater than the average minimum stress, the average minimum stress is greater than the limiting ratio though the target is 275 psi greater, and the average fracture gradient is about 0.62 psi/ft. The strain coefficients are determined in MU-ESW1 (Table 3) since the data in this well is the most recent and then confirmed in the other wells.

Table 3: Fit values for horizontal stress estimates

ε_h	ε_H	Avg. minimum stress (psi/ft)	Avg. magnitude above limiting ratio (psi)	Avg. maximum stress percent of minimum (%)
3.49E-5	8.33E-5	0.63	577	109.9

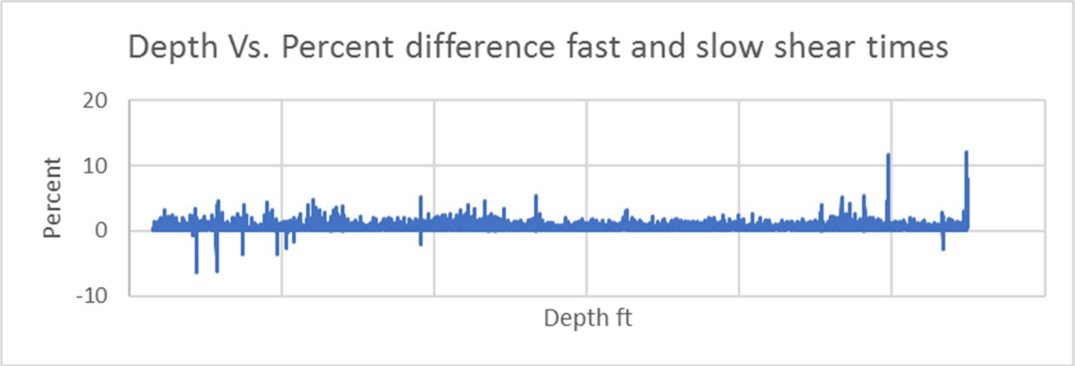

Figure 20: Fast and slow shear sonic anisotropy in MU-ESW1

Since dipole sonic anisotropy is very small (<5% on average) (Figure 20) and laboratory data shown in Table 2 indicates little to no difference in vertical and horizontal Poisson's ratio and Young's modulus, only the vertical values of these properties determined from well logs are used. Using these parameters, the minimum horizontal strain is a positive number less than the maximum strain which makes sense, however, the values of strain in this equation act more as simple fit coefficients as it is impossible to accurately capture the strain of a complex geological unit cut by plutonism and faulting (Blanton et al., 1997). Since the resistivity logs in MU-ESW1 are relatively low (4-foot radius of investigation resistivity is below 2000 Ohm-m) and the ratio of Vp/Vs is relatively high (average of about 1.83) we use 1 for α (Moos and Barton, 1990). Pore pressure is hydrostatic, and overburden is taken from the log density data. The minimum stress gradient used to constrain the stress estimates is assumed to be the fracture gradient and is calculated using the estimated minimum stress from equation 3-7:

$$FG = \frac{\sigma_h}{depth} psi/ft \qquad (3-9)$$

Normally an estimation of the fracture gradient includes the tensile strength of the rock, however, the image logs show multiple fractures that are not sealed, thus jacking pressure should be very near the minimum horizontal stress (Figures 22 & 23).

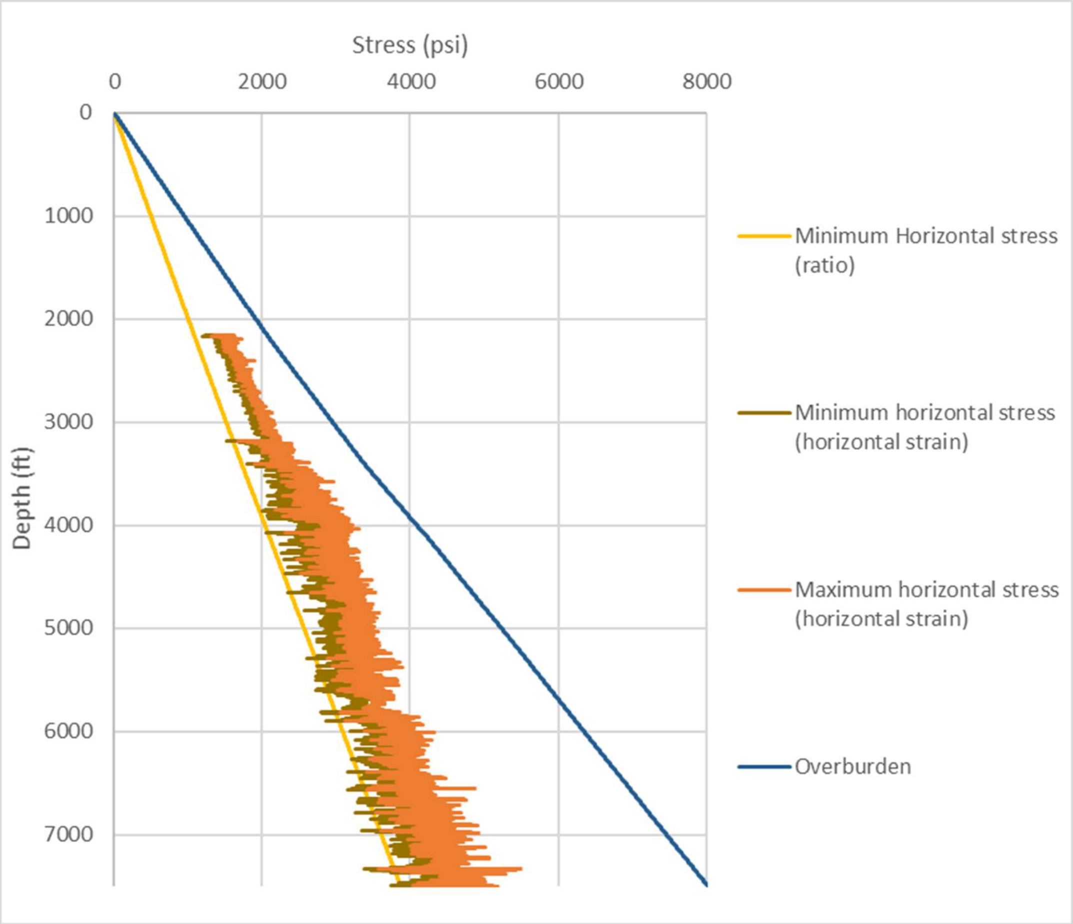

Figure 21: From left to right: limiting stress ratio, minimum horizontal stress estimated from log data, maximum horizontal stress estimated from logs, and overburden from the density log

No breakouts were indicated prior to the injection tests (Figure 22). However, multiple drilling induced fractures were indicated. After the injection test, MU-ESW1 was logged again and possible breakout features were identified (Figure 23).

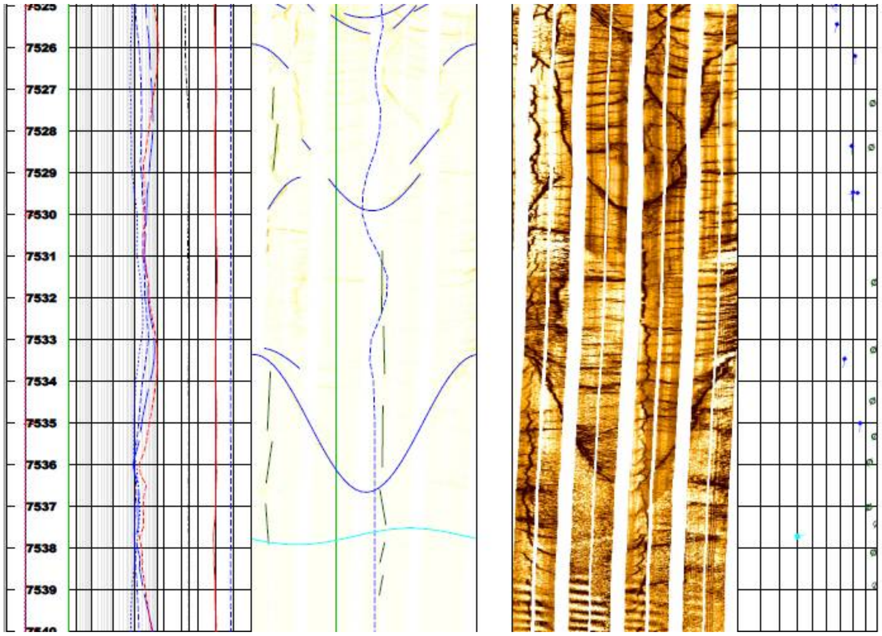

Figure 22: MU-ESW1 FMI log before injection test

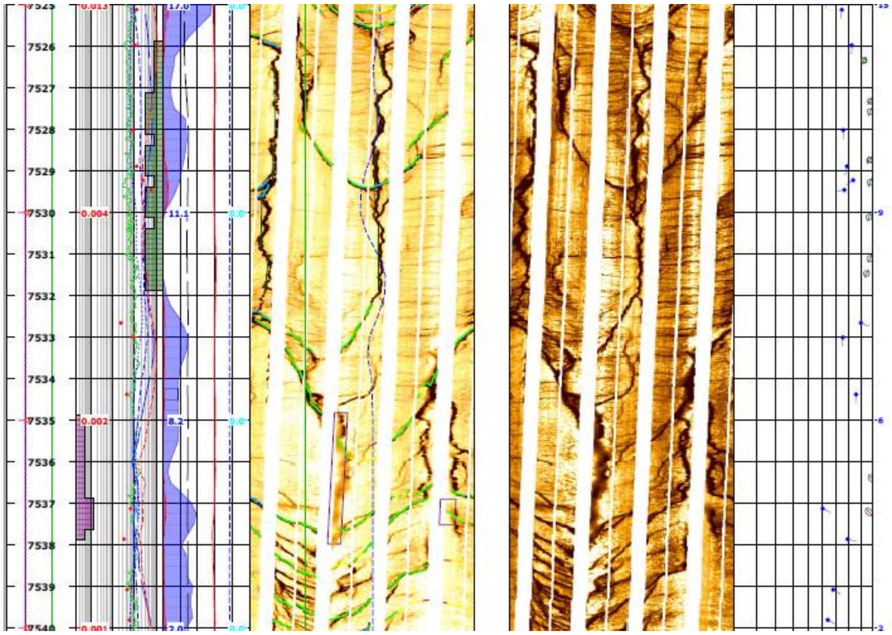

Figure 23: MU-ESW1 well FMI log 7525-7540 ft after injection

Nine locations of drilling induced fractures in MU-ESW1 from 3732 ft to 7538 ft shown in Table 4 were used to establish bounds on the estimated stresses using Kirsch's equations. Equations (2-4) and (2-5) are solved together to generate the values for minimum and maximum horizontal stress bounds listed in Table 4. Values for rock strength are taken from the MU-ESW1 well logs.

Table 4: Depths of tensile fractures and stress estimates applying Kirsch's equation

Depth (ft)	UCS (psi)	UTS (psi)	Pore Pressure (psi)	σ_h (psi)	σ_H (psi)	σ_h limiting ratio	Azimuth (°)
3732	14966.42	1495.3391	1617.076	<2927	<7042.58	>1994.5	216.2, 30.1
4140	17549.6	1740.45	1793.862	<3334.89	<8157.4	>2220.3	242.8, 43.8
4686	16389.3	1595.42	2030.4	<3480.78	<7976.96	>2515.85	51.1, 235.6
4956	16534.3	1595.42	2147.4	<3615.9	<8148.34	>2662.28	357.6, 181
5477	16099.2	1595.42	2373.18	<3787.3	<8210.95	>2943.29	219.8, 32.7
6034	17259.5	1725.949	2614.5	<4124.71	<8871.07	>3243.68	15.7, 198.3
6517	16722.851	1667.934	2823.8	<4288.68	<8886.38	>3504.3	17.5, 203.7
7093	15257.97	1522.896	3073.4	<4409.56	<8604.78	>3814.8	200, 23.7
7538	16490.791	1649.0791	3266.215	<4709.16	<9244.13	>4055.47	209.2, 26.3

Applying this additional restriction in well MU-ESW1, the minimum horizontal stress calculated (Figure 24) falls below the maximum allowable value and is very near the minimum allowable horizontal stress estimated from faulting theory. This is to be expected since the area in the vicinity of the hot springs is seismically active.

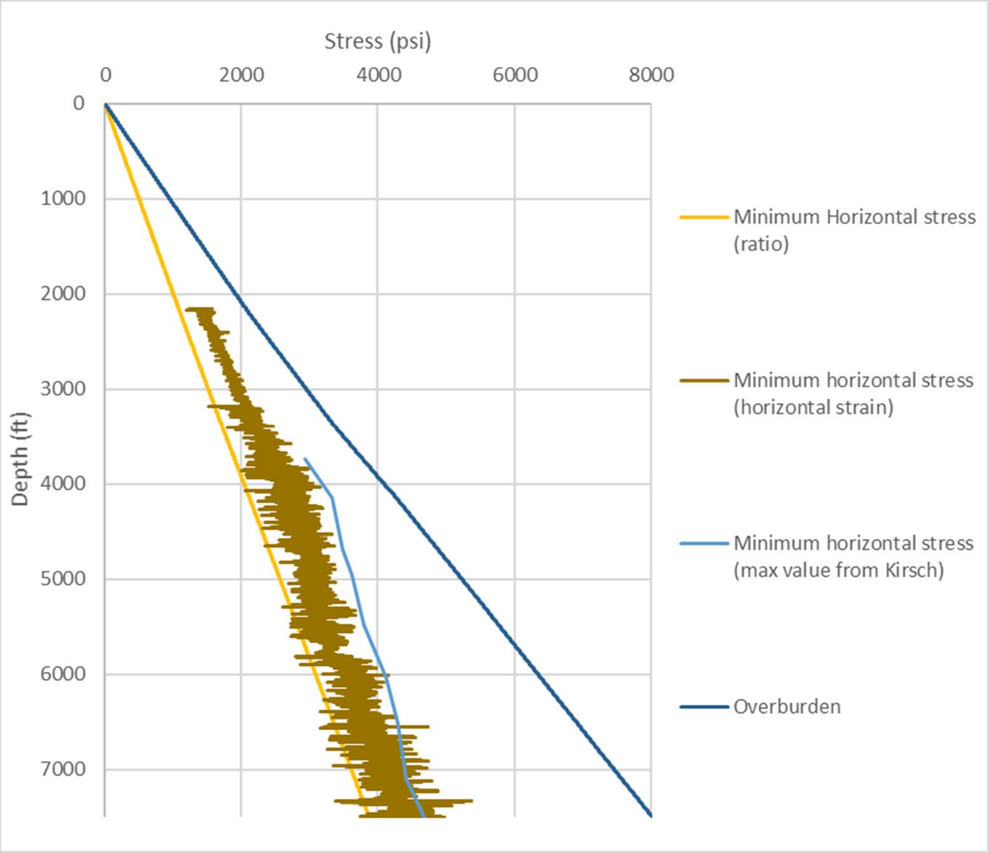

Figure 24: From left to right: limiting stress, minimum stress estimated from well logs, maximum possible minimum stress estimated from the presence of drilling induced fractures and the absence of breakouts. This method solves Kirsch's equations together as inequalities to determine valid ranges of horizontal stresses

3.3 Lithological Grouping: Mechanical Stratigraphy

The FORGE site is located just west of the mineral mountains (Figures 1 and 2) in an area containing a thin layer (~2000 ft) of alluvium and a granitic basement composed of lava flows and plutons.

3.3.1 Alluvium description

The upper geological layer at the FORGE site is composed of alluvium derived from the erosion of the Mineral Mountains intrusive phases. The alluvium in the valley penetrated by Acord 1-26 shows high clay content (Shanon et al., 1983). Not much data is gathered in the alluvium since it is of little interest for the reservoir development operations. We therefore place alluvium into one mechanical unit (Figure 25).

3.3.2 Granite description

The Mineral Mountains are composed of a variety of intrusive rocks including granite, grano-diorite, quartz monzonite and diorite. These rocks were emplaced in several waves and many have distinct characteristics such as grain size differences or fabric (Nielson et al., 1986). The rock samples obtained from MU-ESW1 reveal diorite, grano-diorite, and granite. The reservoir host rocks are composed of granite and grano-diorite. The rocks at the base of the well clearly have a fabric as described by Nielson et al. (1986).

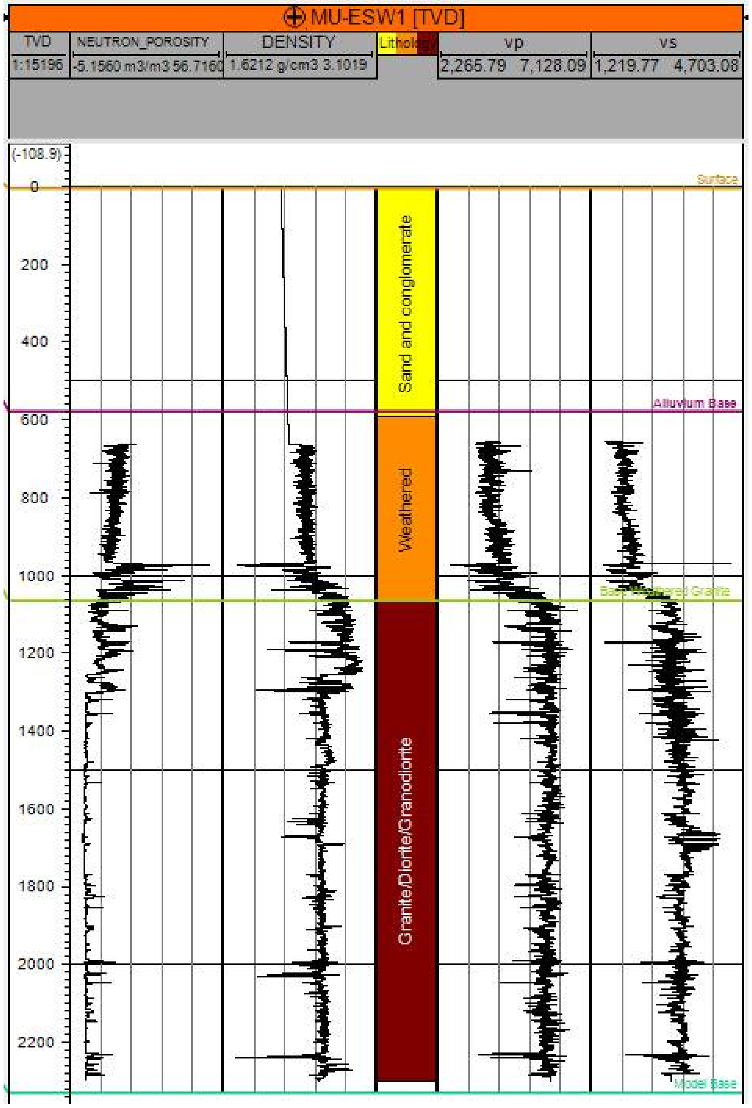

Figure 25:MU-ESW1 mechanical stratigraphy picks

It is clear from the logs that the upper 450 meters of the granite is mechanically different from the bulk of the reservoir (Figure 25). Densities, sonic velocities and the elastic moduli are slightly lower in this upper layer. This layer is considered to be Diorite and weathered granite and separated into its own unit for simulation purposes. A similar layer is visible in logs from all the deep wells in the field except for Acord 1-26 which does not penetrate deeply in to igneous rock and 82-33 whose logs contain too much noise. The rocks beneath the upper layer has lower porosity, faster sonic velocities, slightly higher density, and higher elastic moduli in common. This layer contains the reservoir rocks and is the largest simulation layer.

3.4 Building the Structural/Geologic Model

3.4.1 Geology

Three main rock types are present in the mineral mountains: volcanic rocks, intrusive rocks, and sedimentary rocks. Andesites, lava flows, tuffs, and obsidians present throughout the mineral mountains comprise the extrusive volcanics (Coleman et al., 1997). Three separate groups of intrusive rocks are recognized: 1.) mixed diorite and hornblende granodiorite 2.) gabbro to high-silica granite (more than 90% of granite outcrops) 3.) intrusion of rhyolite, basalt and mixed rhyolite-basalt dikes (Coleman et al., 1997). The second intrusive phase composes the reservoir rock for the FORGE site. It is composed of coarse grained, biotite-hornblende quartz monzonite, porphyritic quartz monzonite and granite mixed with a diorite of similar age (Coleman et al., 1997). The dikes are useful as structural markers. Sedimentary rocks in the mineral mountains and near the FORGE site are quartz and feldspar sands derived from weathering of the local plutonic rocks. Because of this, they vary with changes in composition of the nearby outcrops of plutonic rocks.

3.4.2 Structure

The structure of the Milford site is quite complex involving plutonism, 3 main sets of faulting, large amounts of uplift, and a minimum of 20 km E-W extension

(Coleman et al., 1997). High angle E-W striking normal faults, High angle N-S striking normal faults and low angle structures are present in the Mineral Mountains and Milford valley. Mapping efforts reveal these faults' intersection with the surface, however, their behavior at depth is still disputed in many cases.

The Opal Mound fault is a north-south high angle normal fault on the western flank of the mineral mountains which defines the eastern edge of a small horst (Faulder, 1991). It is the youngest fault in the RHS area. It derives its name from the opaline deposits where the fault is exposed which indicate recent hydrothermal activity. The fault marks the western boundary of the Roosevelt hot springs and appears to act as a dam-like structure preventing hydrothermal fluids from penetrating the valley (Faulder, 1994; Gwynn et al., 2016). Evidence for this is the rapid decrease in temperatures farther into the valley. The dip direction of the Opal Mound fault is thought to be east into the mountain range (Faulder, 1991). Unfortunately, the opal mound fault is not visible on any seismic data collected to date. Its northern termination is somewhere around the intersection with the Negro Mag fault, but cross cutting relationships have not been established. The strongest evidence for this end point is the seismic activity which is very noticeable in the RHS area, but drops off past the Negro Mag (Nielson, 1989).

The negro mag fault is a sub-vertical fault-like structure which cuts the Mineral Mountains E-W and marks the middle of a small graben structure 4-6 miles across (Faulder, 1991). Slip along this structure is thought to be oblique slip with a large component of right-lateral shear (Faulder, 1991). The Negro Mag is the northern boundary of the RHS as shown by decreased temperature and seismic activity to the north. The new Utah well MU-ESW1 was drilled directly in the path of the Negro Mag fault yet it did not encounter any fault like structures or zones of high porosity/permeability (i.e. mud loss zones) (EGI, 2018). This suggests that the Negro Mag fault terminates at or near the Opal Mound fault. Its eastern extent is not well defined. Unfortunately, the Negro Mag too is not visible on seismic data gathered thus far.

Low angle structures are present in the mineral mountains especially near the RHS. Two types of denudation structures are observed: 1.) faults separating sedimentary rocks from plutonic rocks 2.) faults cutting plutonic rocks of the Mineral Mountains. The best example of the first style of faulting is the remnants of the Cave Canyon detachment in the southern part of the range (Nielson et al., 1986). Examples of the second type near the RHS are the Salt Cove and Wildhorse Canyon structures. These structures are marked by zones of cataclasite up to 12 feet thick (Faulder, 1991). Barker (1986) interprets a possible low angle structure in the granite off the western flank of the mineral mountains (Figure 26):

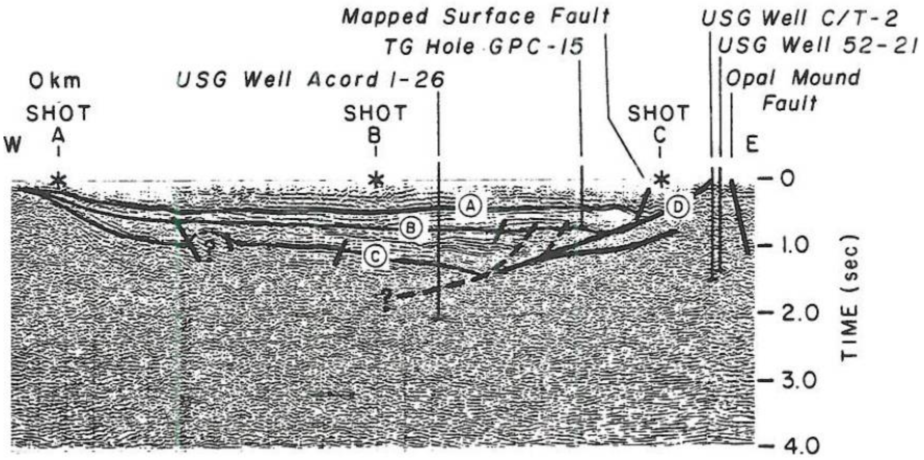

Figure 26: Seismic interpretation of Milford Valley (Barker, 1986)

Sibbett and Nielson (2017) mapped several curvilinear normal faults in the sediments west of the Mineral Mountains in Milford valley (Figure 27), however, seismic data and gravity data indicate that they do not intersect the granite basement.

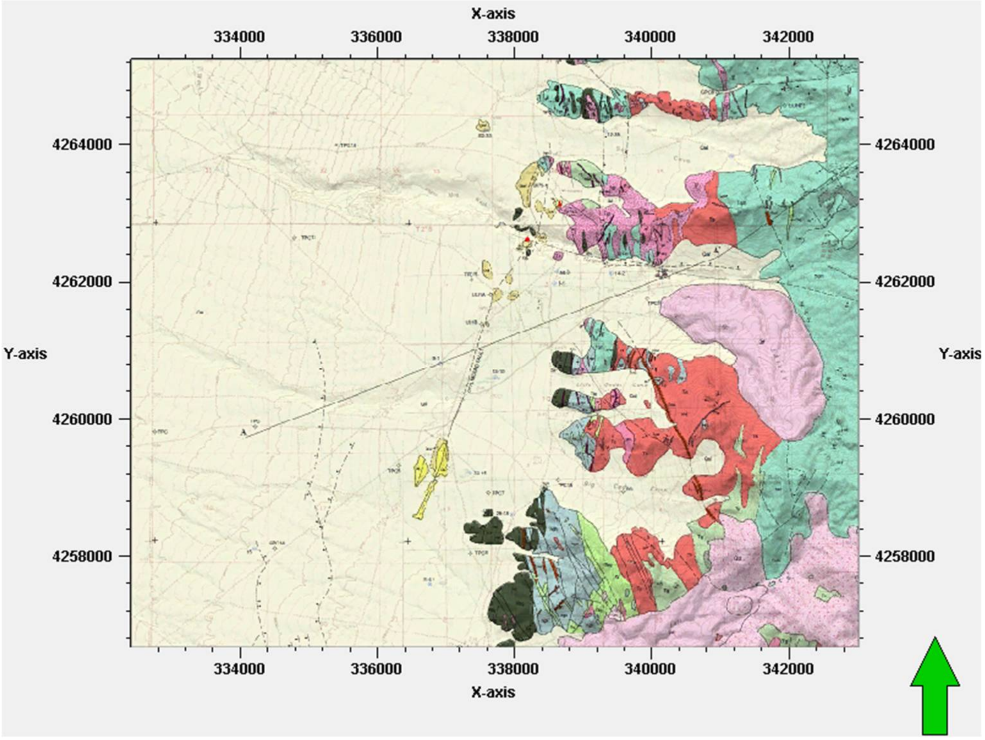

Figure 27: Geologic map of the Mineral Mountains showing curved normal faults on the bottom left (Sibbett and Nielson, 2017). Based on seismic data, these faults do not appear to cut into the basement.

Combining all available data sources results in a granite-sediment contact in the FORGE site that is not appreciably offset by faulting though faults likely exist in the granite as seen in Figure 26.

3.4.2 Simulation Grid

Though little to no offset is present in the model area, the Opal Mound and Negro Mag faults are gridded into the model. This enables data to be exported from the grid into other workflows with markers for the faults.

Since this model is intended to be an input for a variety of uses such as thermal modeling and hydraulic fracture modeling, its areal extent and depth are chosen to satisfy the requirements of these models. The total depth of the model is 1,500 m below sea level and its areal dimensions are 7,780 m x 8,510 m. The coarse grid used herein focuses on regional thermal modeling applications and regional visualization of stresses and properties. For localized stimulation applications, the grid and size of the model can be easily reduced in size.

Selection of the cell size is a key decision that must be made. It is very easy to simply overlook major contributing features by selecting cell sizes that are too large and average their effects out of the model. Ordinarily, the cell size should be at a maximum the dimensions of the smallest feature the model intends to capture. There are several bases in this model on which to select the areal cell dimensions such as natural joint spacing, hydraulic fracture spacing, areal extent of coarse/fine grained changes in granite composition, thicknesses of cataclasite zones (10m>thickness (12 ft)), and thicknesses of dikes (20 m from map). However, since properties are relatively uniform, we select x-y dimensions of 100 m.

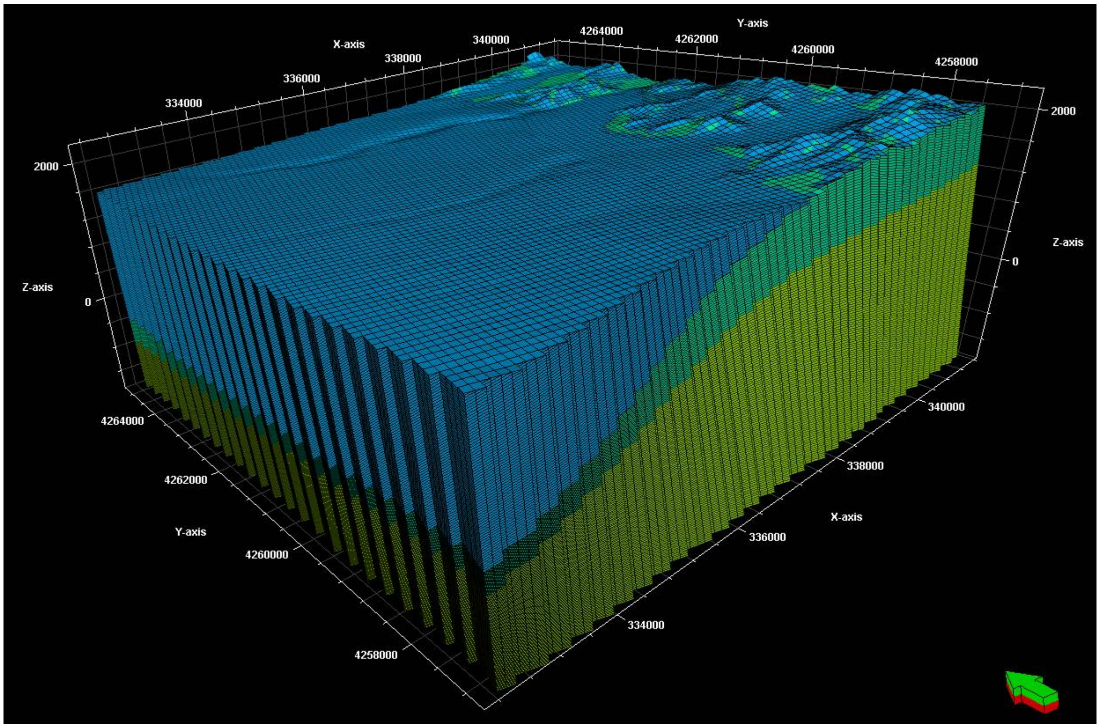

Figure 28: 3D model displayed with three major units and grid cell dimensions

The layering scheme chosen in the upper sedimentary zone follows the granite contact simulating deposition due to erosion and basin subsidence. The layering in the lower two units is proportional dividing the space at a given pillar into even segments between the upper and lower layers. The alluvium was divided into 25 m layers, the weathered granite was divided into 25 layers, and the massive granite was divided into 90 layers. The average thickness of all the cells combined is 25 m. Since there are no small features of importance around the reservoir and the granite is considered homogenous and isotropic, slight variations in cell heights are neglected.

3.5 Property Modeling

For the interpolation of mechanical parameters stochastic methods are used. Since the properties to be modeled such as porosity and density exhibit relatively low fluctuations except where borehole enlargement or fractures are identified, interpolation methods such as inverse distance should provide smoother distributions.

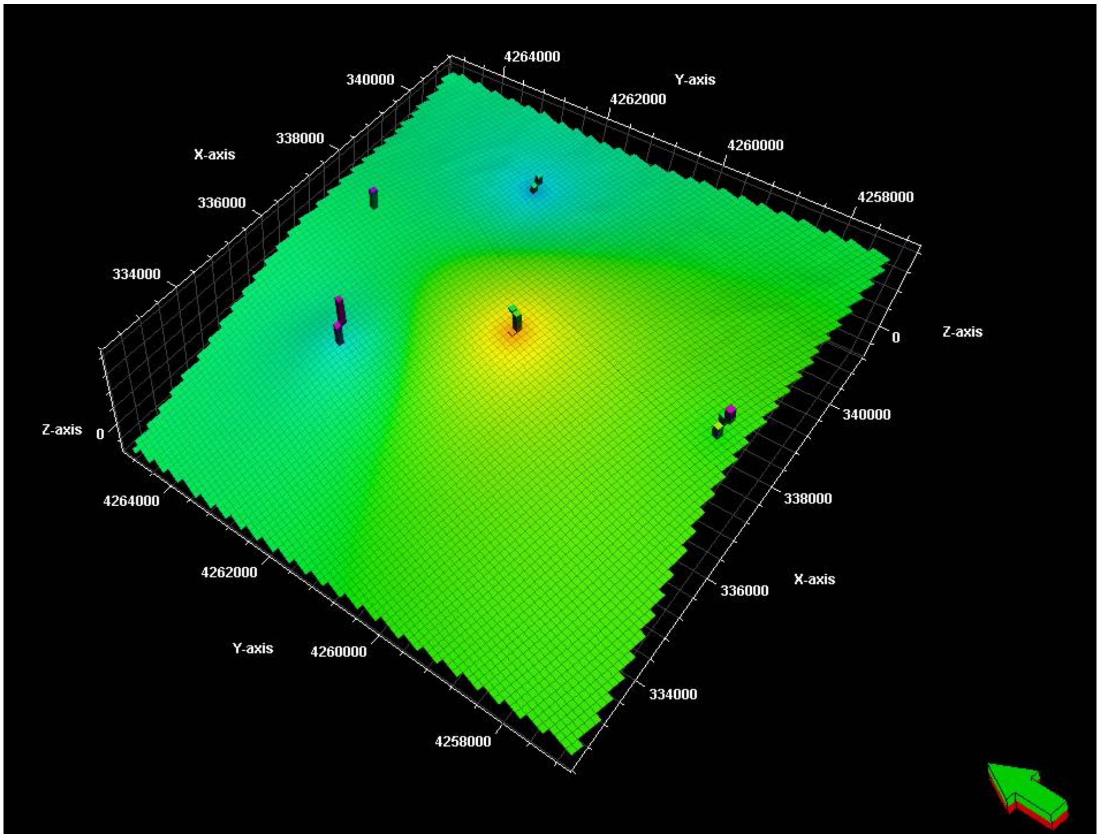

Figure 29: Inverse distance weighting of data to interpolate density; bull's eyes around wells are undesirable

However, this method generates bull’s eye features around wells as seen in Figure 29. Therefore, Sequential Gaussian Simulation (SGS) is the selected method in this project. SGS uses Krigging, a linear weighting method of data interpolation, to estimate data points using hard data. Estimated data points are subsequently used in the estimation of new data points. Linear weighted methods of interpolation such as Krigging yield smooth results that fit all the hard data. However, if only Krigging is used, bull's eye structures can result (Figure 30) similar to those in Figure 29.

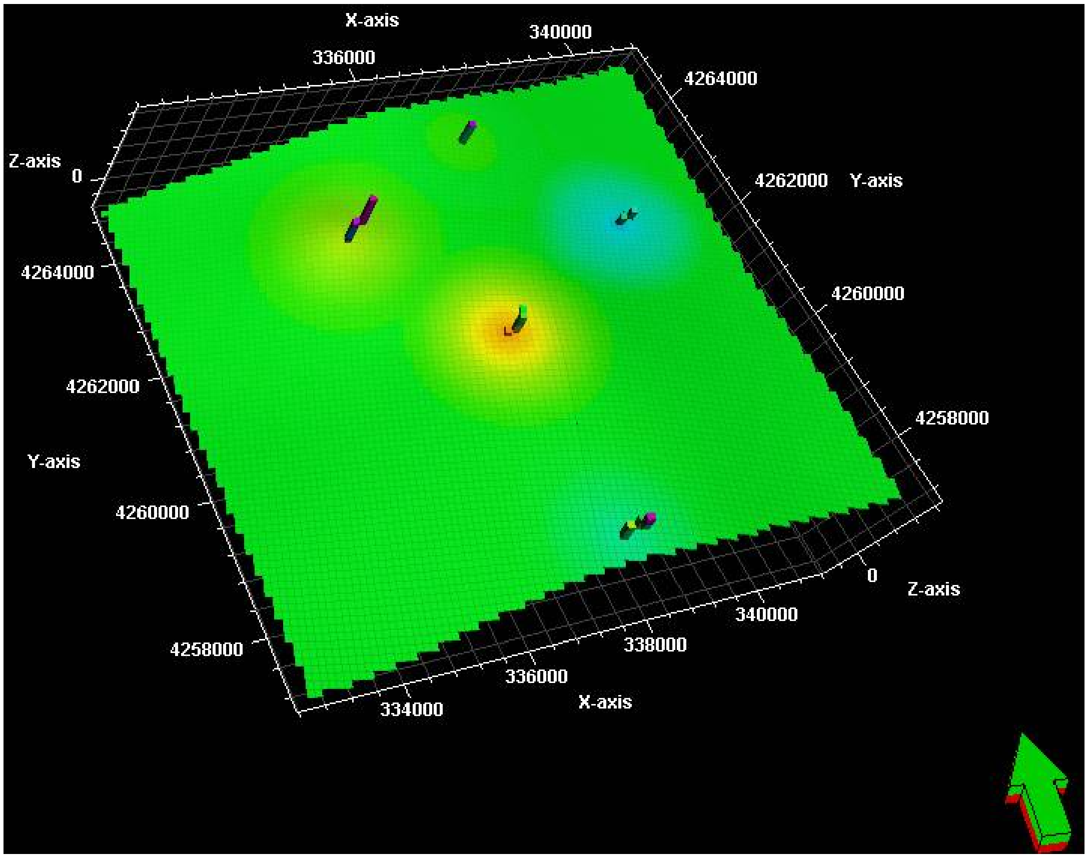

Figure 30: Slice of Krigged density model

Stochastic methods result in models that fit the original data but include more variability. For properties such as porosity, density, and sonic velocities that are known to have small scale variability across the field, this approach better captures the extremes of possible values. The inputs to this algorithm are the upscaled properties along the well logs and the variogram ranges. The well logs are upscaled using the arithmetic mean of well log values within the segment being upscaled. This is because there are no variations in lithology considered in the model which could provide constraints for the upscaling process. The vertical variogram inputs (sill, nugget, and range) (Figure 31) can be selected directly from well data, however, the horizontal ranges cannot be chosen this way. The nugget is chosen as zero for all the property models in this work. A nugget of zero corresponds with a more homogenous spread of properties as might be expected in granite.

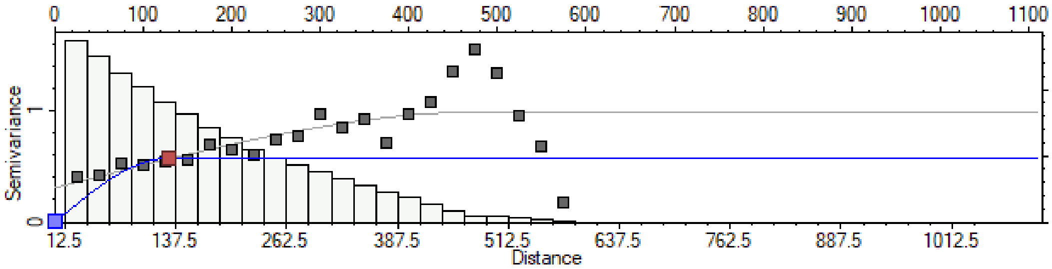

Figure 31: Example vertical variogram from the upscaled 3D density data

Normally, macro scale features might dictate the selection of the horizontal ranges, however, the granite is considered homogenous and isotropic, thus the ranges are chosen based on well separation. Table 5 shows the distance to the closest well from each well. The horizontal range will be chosen as half the distance to the nearest well for 52-21 since its nearest neighbor is the farthest away (3190 m in Table 5 below) of the modeled wells. Both range values will be the same at about 1600 m (3190/2).

Table 5: Horizontal Well Separations

	1-26	52-21	9-1	14-2	82-33	MU-ESW1
Nearest well (m)	5700	3190	2568	2600	2547	2547

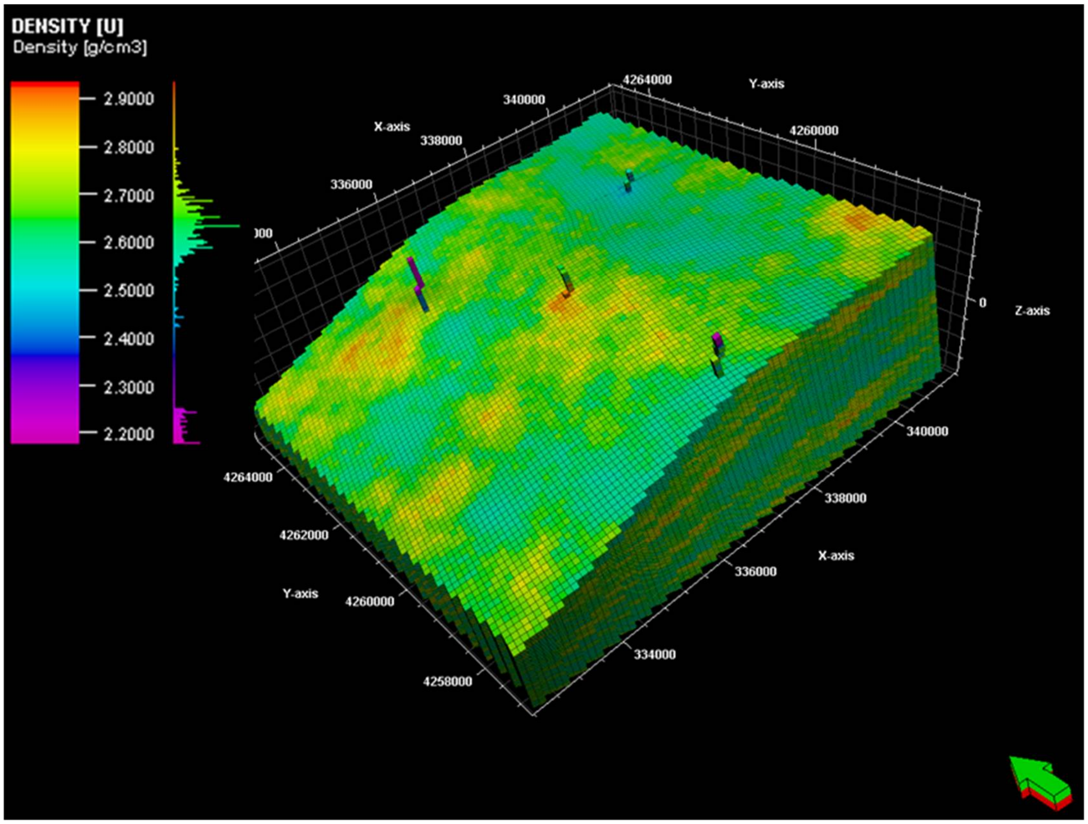

Figure 32: 3D density model of the granite reservoir volume (bottom zone modeled). The four columns of cells indicate locations of well data.

The 3D property volumes generated are then examined to determine if they are a reasonable representation of the well data. The 3D density volume is shown as an example above (Figure 32). The histograms from the well logs and upscaled well logs are used to assess the results based on the inputs (Figure 33). The histogram for the density model clearly shows a tendency of modeled values to congregate about the mean of about 2.6 g/cc. This is caused by outlying data being averaged out of the upscaled well logs. Another likely cause is the large range values; if the simulation looks over a long distance to correlate, simulated values will tend to be average. Since lab data indicate the matrix in the area is granite with a very tight distribution of properties, the simulation eliminating outliers is actually a more realistic model.

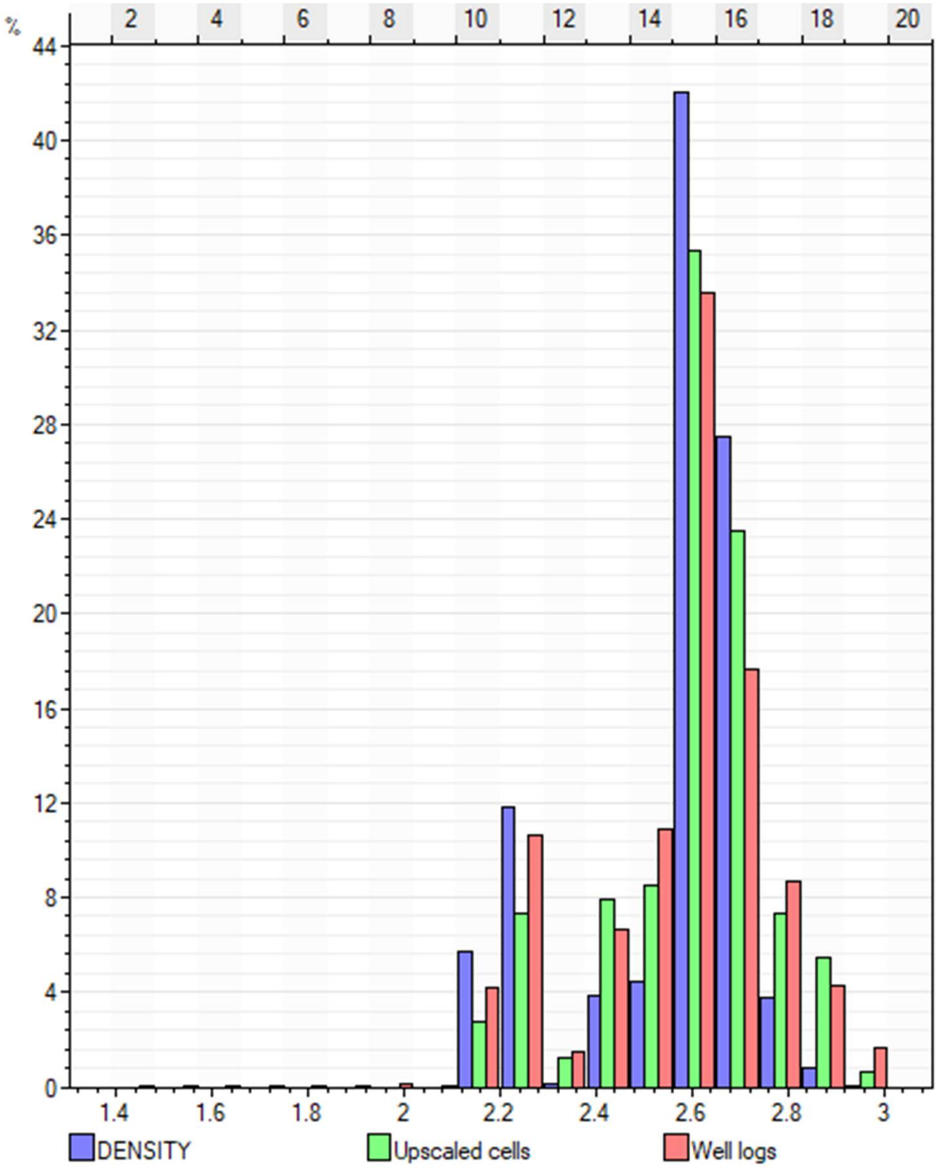

Figure 33: Histogram showing input well log data (pink), upscaled data (green), and simulated data (purple). The higher percentage of simulated values around 2.6 g/cc is caused by outlying well log values being upscaled out of the data set. This is not a concern since these values are in most cases due to fractures or borehole enlargement.

Models for Neutron porosity and sonic compressional and shear velocities are generated in the same fashion. Then, using equations 2-17, 2-18 and 3-3 the dynamic and static Poisson’s ratio and Young’s Modulus are calculated in each cell using the calculator feature in Petrel. The UCS is calculated similarly using equation 3-1. This ensures the values in each cell are consistent with other in-situ values; this is important since the in-situ values will be used to estimate stresses. Using this approach also introduces some of the small-scale variability that is almost certainly present into the in-situ estimations.

3.6 In-situ Stress Modeling from 1D MEMs and Direction Determination

3.6.1 Modeling in-situ stress from 1D MEMs

The overburden is calculated in the 1-D MEMs using the density logs and is used in developing stress estimates along the well bores. In the previous step the density values are interpolated through the 3D modeling volume and then used along with a depth property to estimate in-situ overburden stresses consistent with the density model.

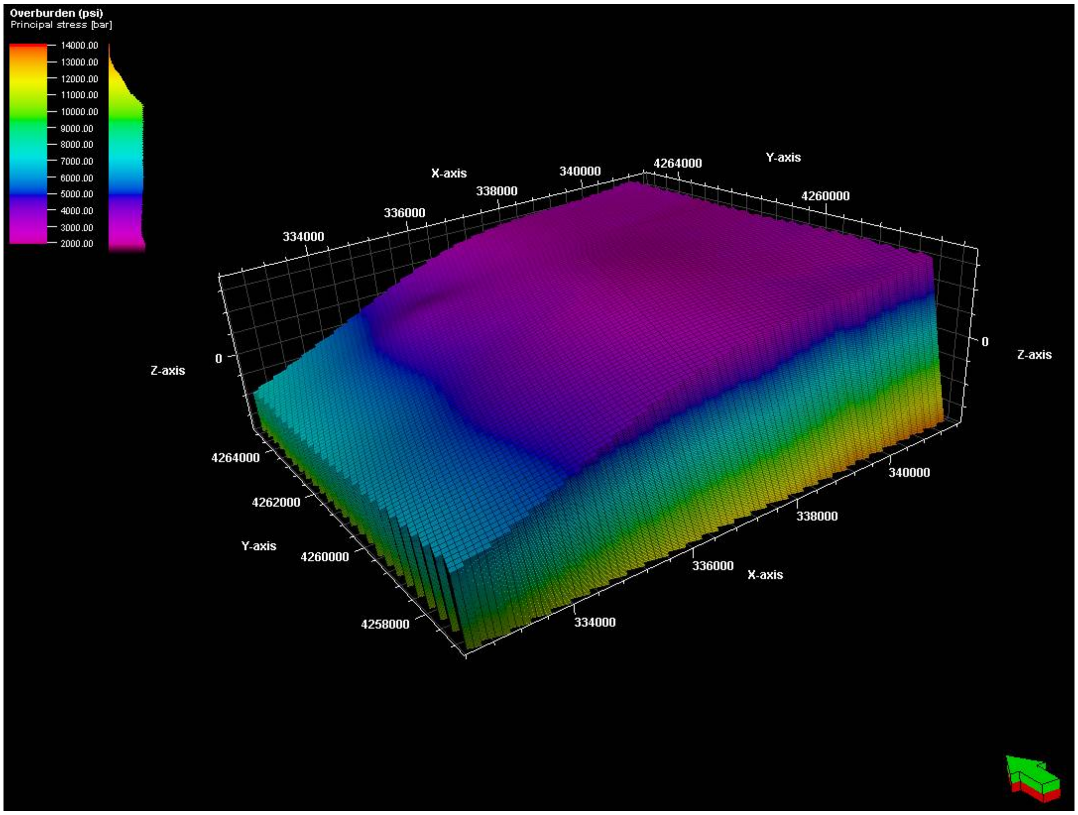

Figure 34: Overburden calculated from the depth and density models in the lower massive granite portion of the model.

The pore pressure is calculated using a property that calculates the depth to the center of each cell from the surface of the model. Pore pressure is estimated to be hydrostatic. Now using the models simulated for pore pressure, overburden, static Poisson’s ratio, static Young’s Modulus, and the coefficients (ε_H=3.49E-5 and ε_h=8.33E-5) for the Poisson’s equation to estimate horizontal stresses (equations 3-7 and 3-8), the horizontal stresses are calculated in each cell using the calculator feature in petrel as in the property modeling section above. The fit coefficients are determined in the 1-D MEM step such that the stresses estimated fall within the limits allowed by the limiting stress ratio and the Kirsch solution.

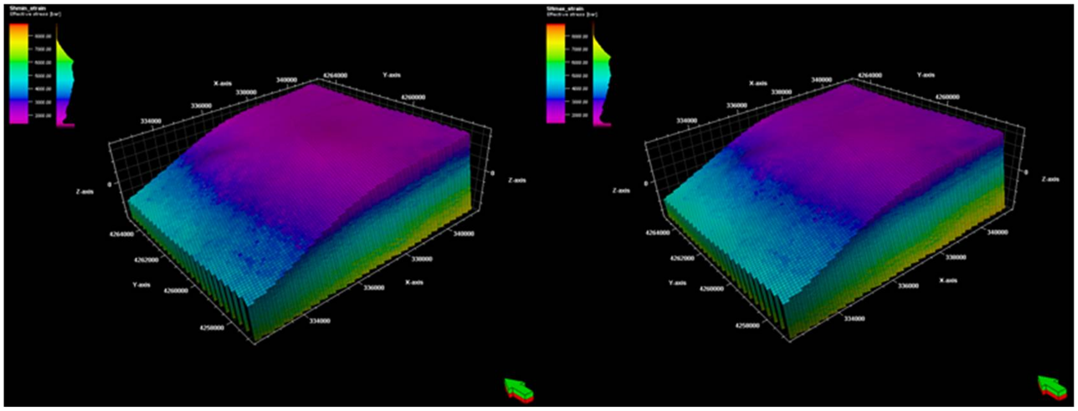

Figure 35: Left: σ_h. Right: σ_H. Estimates use the strain coefficients determined in 1-D MEMs in MU-ESW1. The models look very similar since horizontal stress magnitudes are very close in value.

The horizontal stresses (Figure 35) are within a few hundred psi of one another as revealed by the injection test report in MU-ESW1 (EGI, 2018).

3.6.2 Stress direction determination and interpolation

Stress directions are estimated from breakouts and drilling induced fractures in wellbores as well as fault orientations. The FMI logs in MU-ESW1 show more than 100 drilling induced tensile fractures, however, no breakouts are visible prior to the injection test. There is little change in the local stress directions from regional values since drilling induced fractures in MU-ESW1 reveal the maximum principle stress azimuth is north northeast – south southwest as can be seen in Figure 37 which helps to visualize the range of azimuths indicated by the FMI logs.

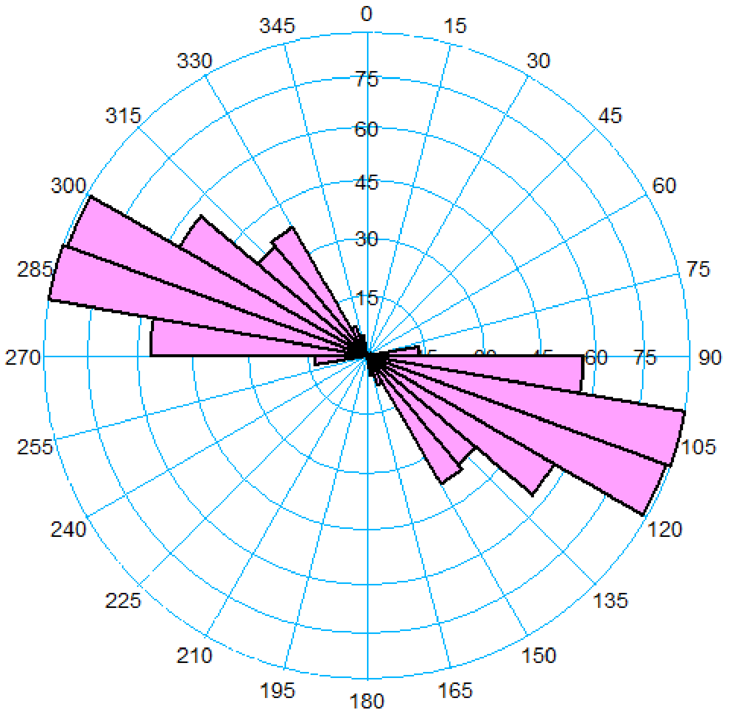

Figure 36: Rose diagram showing strike of planes perpendicular to tensile fractures observed in FMI logs in MU-ESW1. The range of strikes show the variation in azimuth of minimum horizontal stress

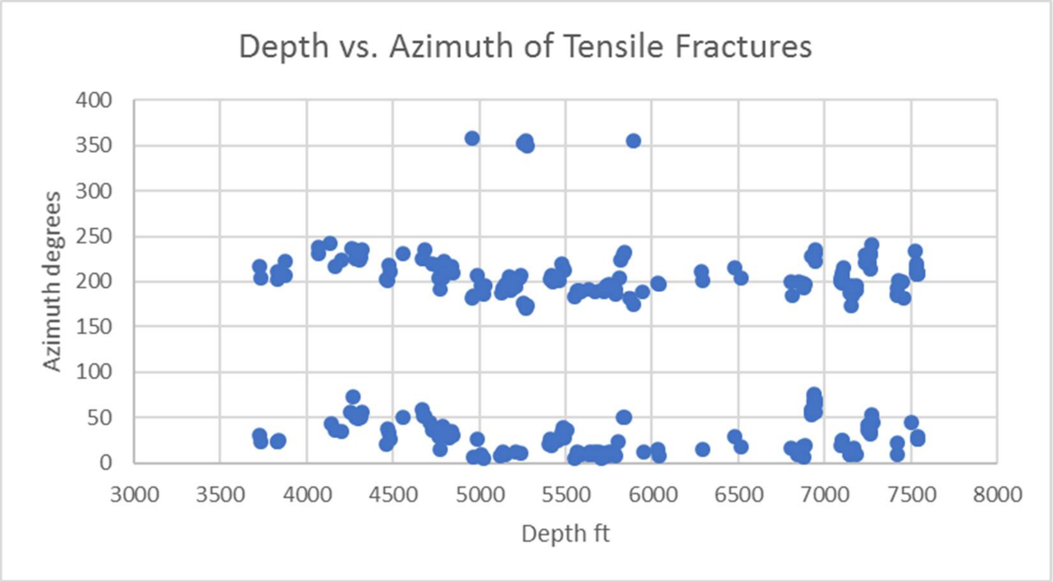

Figure 37: Azimuths of drilling induced fractures showing direction of maximum horizontal stress plotted along the depth of MU-ESW1; the 4 points at the top represent points near 0 degrees. The trend appears to shift in a southerly direction around 5000 feet and then come back to a more southwestern direction

The data thus far indicate stress directions consistent with regional stress directions, however, an important point that needs addressing is the behavior of the stress directions near the well bore with depth. Figure 36 (rose diagram) demonstrates that there is in fact a distribution of azimuths at which tensile fractures occur, but do not yield any information about trends in changes with depth. Figure 37 plots the azimuths of drilling induced fractures along the length of MU-ESW1 to analyze possible trends. There appears to be about a 50-degree change in the direction of maximum horizontal stress from 225 to 175 degrees around 5000 ft and then a slow change back to around 210 degrees at the bottom of the well around 7500 ft. Since stimulation will be focused at the deepest section of MU-ESW1 where the stress directions appear to have a slightly wider scatter, the average azimuth of 25 degrees indicated by the tensile fractures for the maximum horizontal stress will be used.

3.7 Modeling In-situ Fractures

3.7.1 Data analysis

The sources of fracture data for the DFN generated here are FMI log analyses from well MU-ESW1 and outcrop analyses (EGI, 2018). FMI logs were run and analyzed from about 2000 ft depth to the bottom at around 7500 ft. The data was corrected for well bore deviation by Schlumberger in their analyses. The data included drilling induced fractures and bedding planes as seen in Figure 38 on the left (below). These features were removed from the data (Figure 38 right) since our focus is on natural fractures cutting initially intact rock prior to stress field disruption caused by drilling.

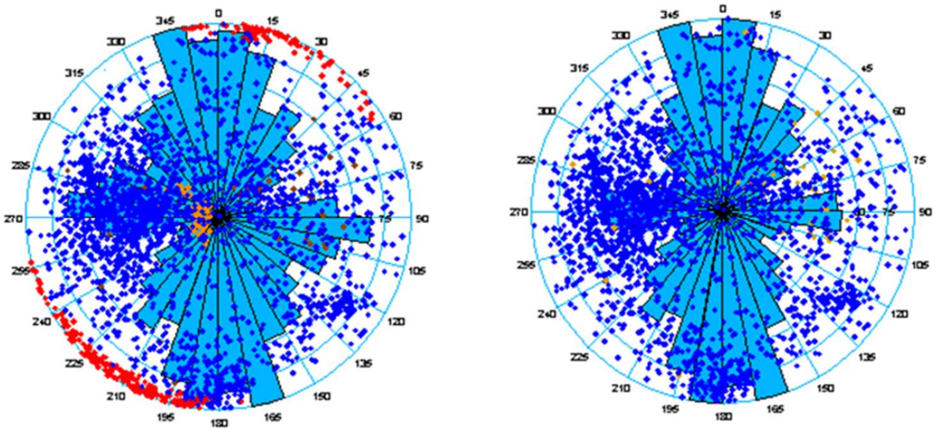

Figure 38: Stereonet plot of fracture data in well MU-ESW1; left plot is all data (red and brown points are drilling induced fractures and bedding planes); right plot is data with bedding plane and induced fractures removed

Faulder (1991) identifies three major joint sets in outcrops in the central Mineral Mountains: two sets of near perpendicular steeply dipping joints trending north and east and one set of shallow to steep westward dipping joints. The stereo plot of fracture data from MU-ESW1 shows three clear sets only one of which fit Faulder’s (1991) description: 1) steeply dipping east-west striking fractures (consistent with Faulder (1991)) 2) steeply dipping northeast-southwest striking fractures (not consistent with Faulder (1991)) 3) steep to shallow east dipping north-south striking fractures (not consistent with Faulder (1991)). The inconsistencies indicate that it is likely that the fracture populations vary across the mineral mountains and with depth. This is probably caused by low angle faulting tilting fractures from their original orientations. A fourth set is used to model the remaining fractures since the tight sets do not cover the fractures of scattered orientation.

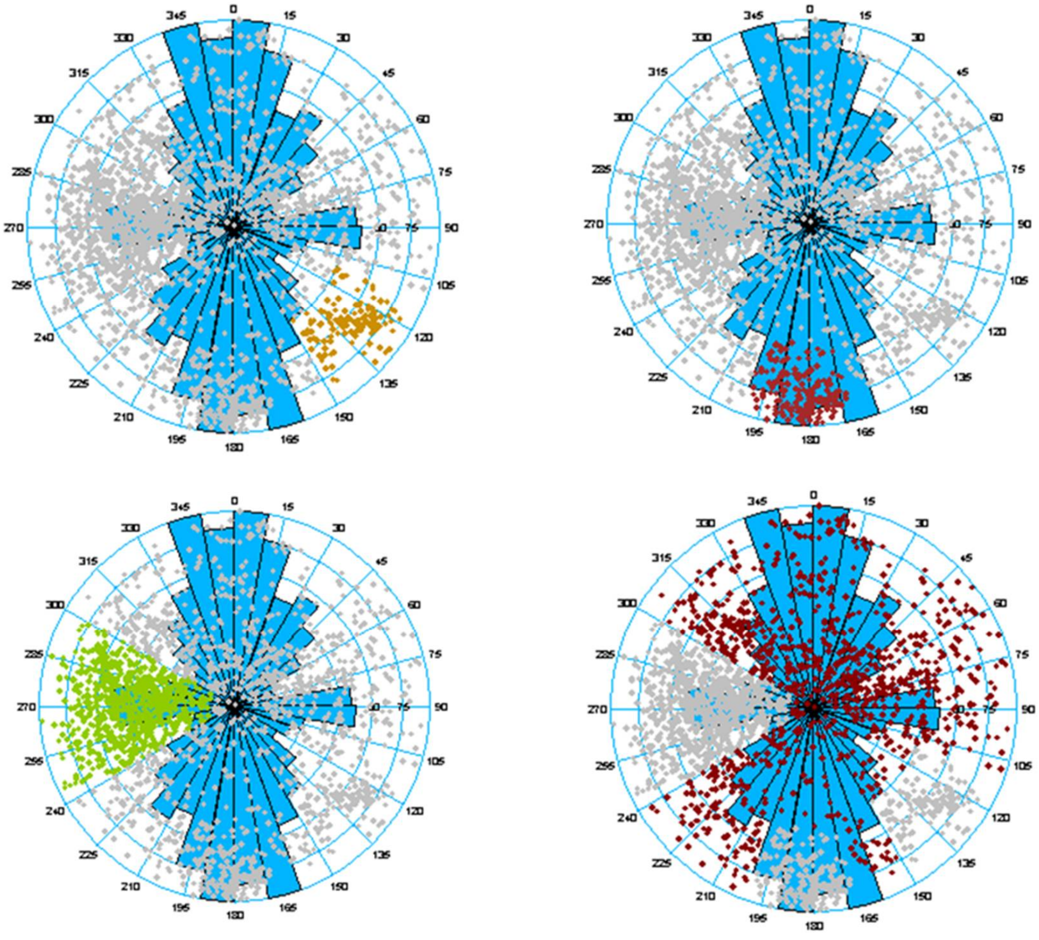

Figure 39: Top left: set 1, top right: set 2, bottom left: set 3, bottom right: set 4

3.7.2 Modeling Inputs/Parameters

The DFN is stochastically generated using Mangrove in Petrel software. One of the major uncertainties in the development of this DFN is defining the lateral distribution density of discrete fractures. The P32 (fracture surface area / rock volume) log for each set was calculated along MU-ESW1. Since no correlation was present between fracture intensity and sonic compressional slowness, sonic shear, density or any other geophysical logs, the input to the 3D distribution model remained the P32 logs along MU-ESW1 for each set. Using Sequential Gaussian Simulation these logs were used to create 3D P32 volumes. Vertical ranges and sills were selected using variograms and horizontal ranges were set to 1600 ft based on well separation as with the other modeled properties. The nugget values were kept at zero. 3D P32 and DFN models were only generated for the bottom zone consisting of massive un-weathered granite since fracture data was only gathered in this zone.

The modeling parameters are listed in Table 6 and Table 7. The mean, standard deviation and max length of the fractures were calculated using outcrop data for a log normal distribution (EGI, 2018). The Fisher model was used to model the angular distributions for each set. This method describes a distribution of angles similar to a normal distribution about the average angle determined from data as in Table 7. The Fisher model uses an input called concentration to determine how tightly or loosely the simulated angles are distributed about the mean. Low values of concentration create very distributed simulated angles while high values create populations very close to the average dip and dip azimuth. Higher concentrations are used in sets 1 and 2 (Tables 6 and 7) since these distributions are tighter. Set 3 contains the shallow to steep dipping fractures so a lower concentration is better suited (broader distribution). Set 4 is intended to be residual fractures which are at random orientations, hence 0 is used to create a very wide spread about the average dip and dip azimuth. Mangrove uses a two-pronged modeling method for in-situ fractures: 1) a 3D cellular or implicit model containing upscaled properties for fractures below a certain length defined by the user and 2) a 3D discrete fracture model containing all fractures greater than the implicit maximum length. We are primarily interested in the discrete fracture model since they can be exported and used in other modeling efforts. Because of this and because a large number (>500,000) of discrete fractures causes display and computational issues, the length at which fractures are relegated to the implicit model is varied until the desired number of discrete fractures are present. In this modeling effort, the total number of discrete fractures is kept below 100,000. For various applications, however, the number of discrete fractures can be increased or decreased as necessary by decreasing or increasing the implicit cutoff length respectively.

Table 6: DFN modeling dimensional inputs and results for each set; inputs from report (EGI, 2018)

	Mean (m)	STDEV. (m)	Max (m)	Number of Fractures	Angle Model Used	Concentration	Implicit Cutoff (m)
Set 1	88.84	74.03	150	3,258	Fisher	50	149.9
Set 2	88.84	74.03	150	9,438	Fisher	50	149.9
Set 3	88.84	74.03	150	13,223	Fisher	20	149.9
Set 4	88.84	74.03	150	7,898	Fisher	0	149.95

The dip angle and dip azimuth parameters shown in Table 7 are calculated based on the highlighted sets shown in Figure 39.

Table 7: DFN dip angle and strike inputs for each set

	Mean Dip Angle (°)	Mean Dip Azimuth (°)
Set 1	63.93	129.66
Set 2	73.77	182.45
Set 3	46.08	270.47
Set 4	43.42	171.08

3.7.3 Modeling Results and Discussion

The results of the simulation are shown in Figures 40, 41, 42 and 43 below. The goal was to re-create each concentrated set and then simulate a light scatter of fractures with set 4. Figure 40 shows the simulated DFN next to the data. Figure 43 shows the individual model of each set.

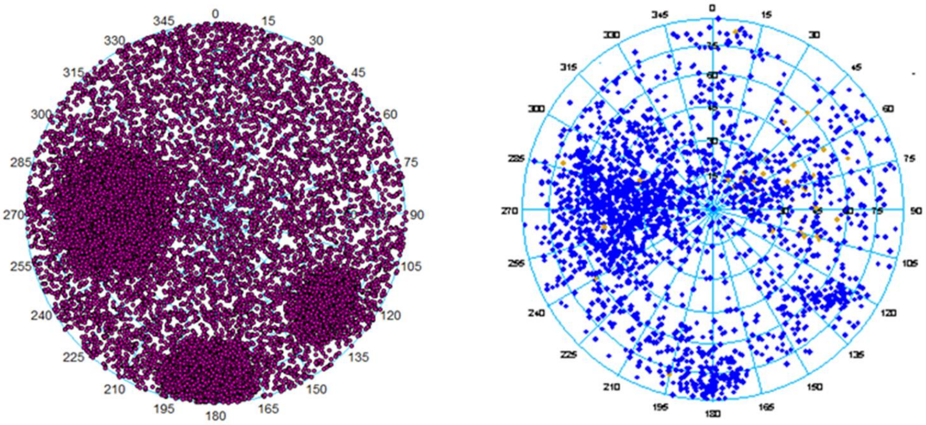

Figure 40: Left: simulated DFN, right: FMI log data

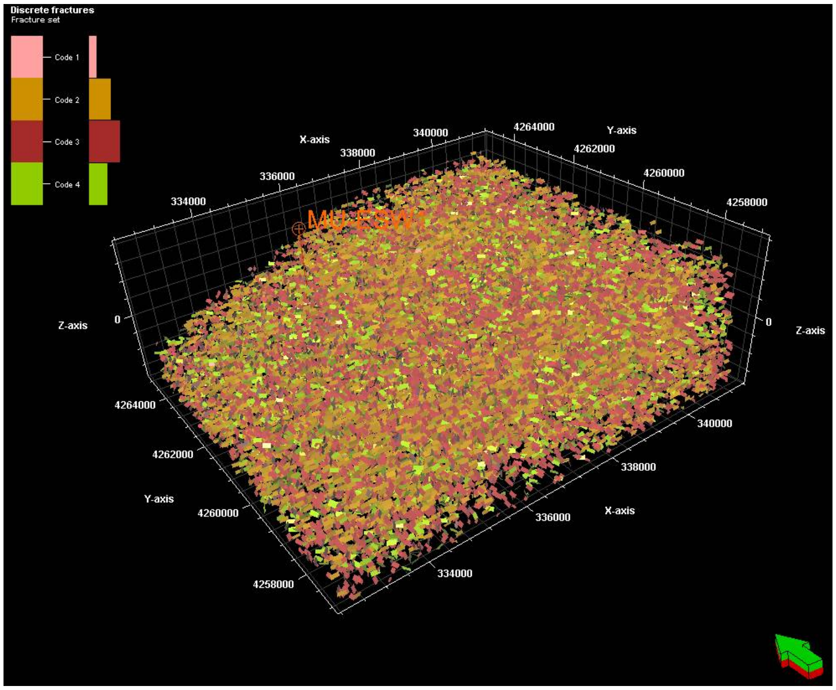

Figure 41: All 4 fracture sets displayed in 3D

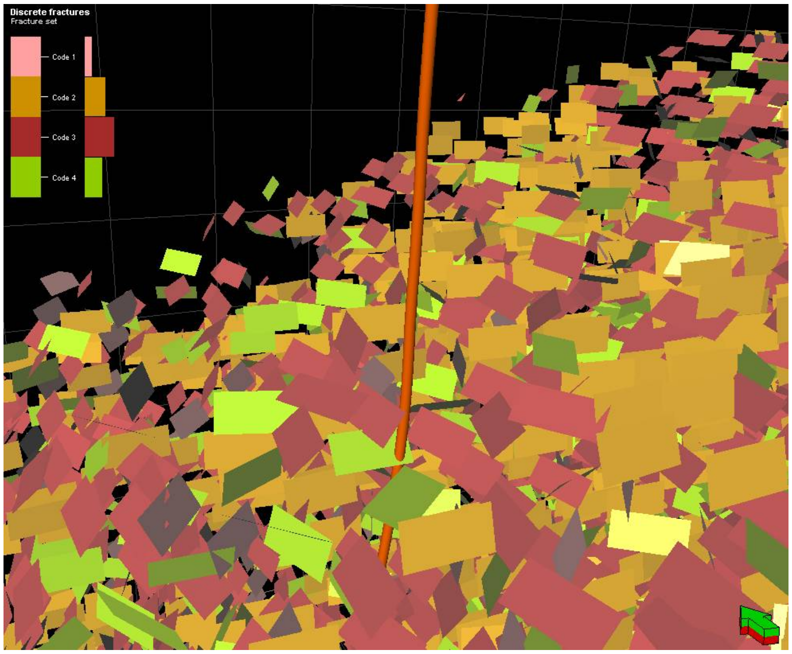

Figure 42: Simulated fractures around well MU-ESW1

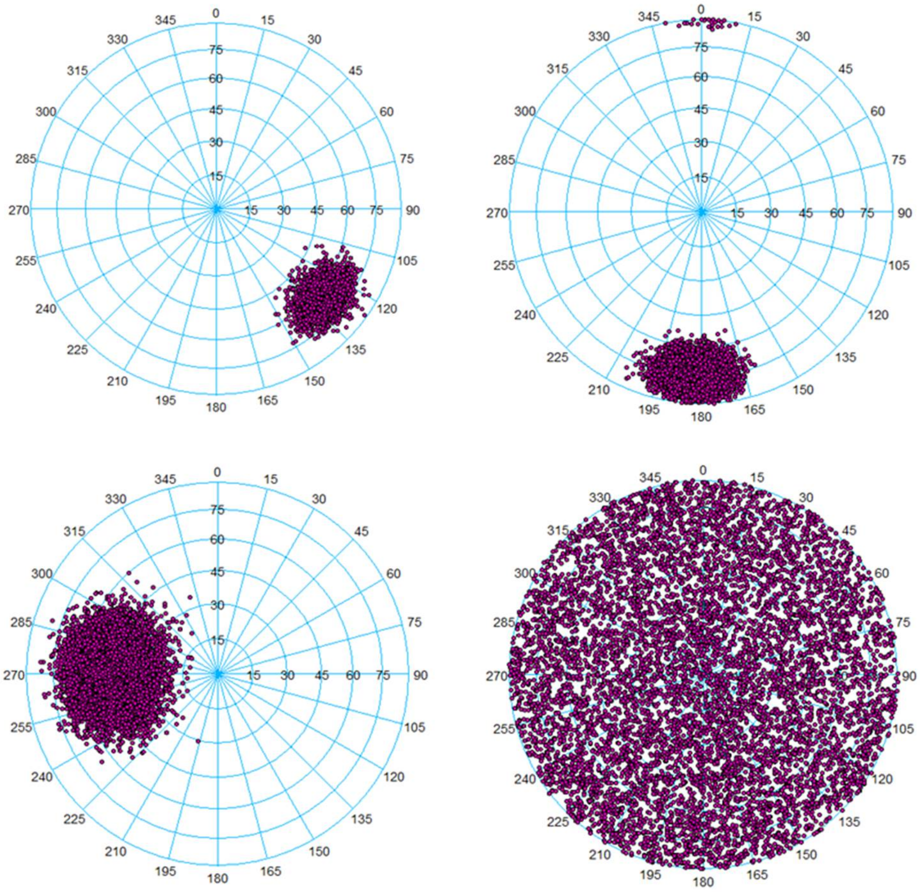

Figure 43: Modeled fracture sets; top left: set 1, top right: set 2, bottom left: set 3, bottom right: set 4

An important objective of developing a DFN is to analyze the quantity and effect of critically stressed fractures. The best approach to this is to calculate the normal and shear stresses on each fracture due to the principal stresses. The ordinary method of doing this is applied to data processing of triaxial laboratory tests. In triaxial tests, σ_2 and σ_3 are the same since confining pressure is uniformly applied while σ_1 is increased:

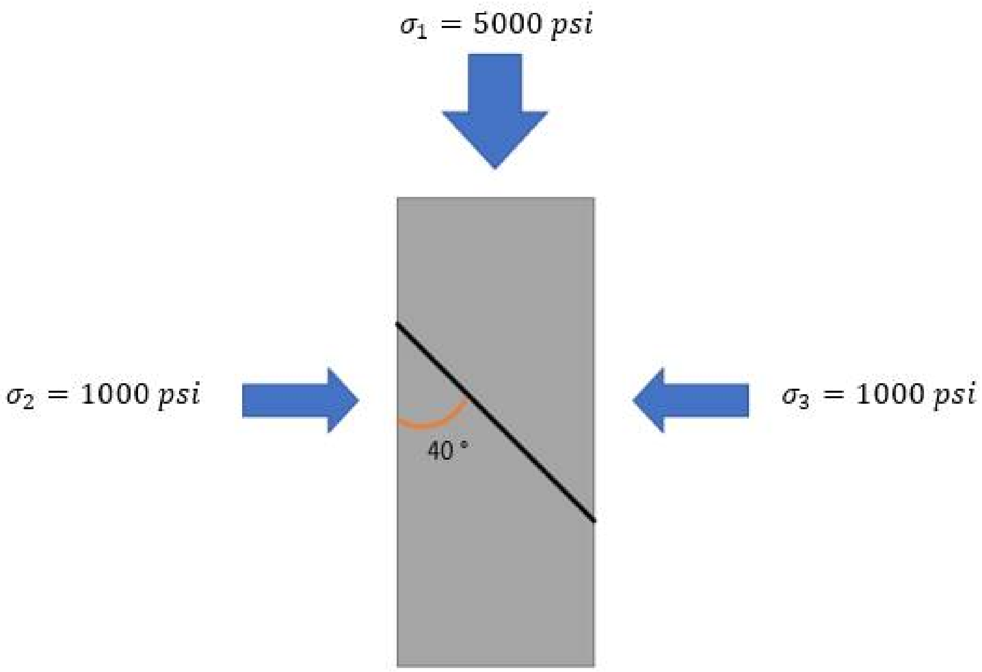

Figure 44: 3D triaxial configuration. Fracture (black line) shown inclined at 40° with respect to vertical. Horizontal stresses are uniform while vertical stress is increased

In this 3D configuration (Figure 44), estimating the stresses on a fracture can be reduced to a 2D problem since σ_2 and σ_3 are identical:

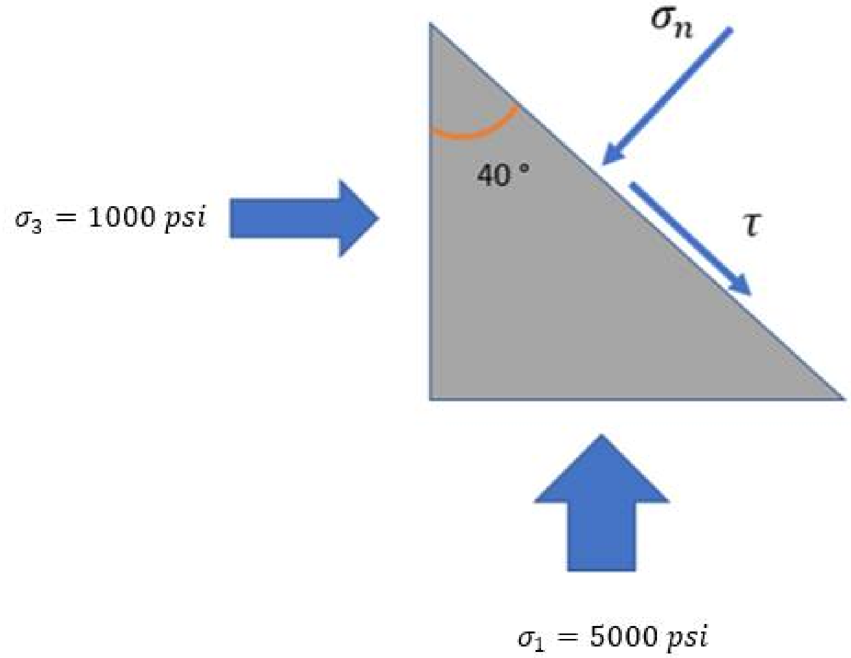

Figure 45: 2D simplification of calculating stresses on a fracture plane in 3D triaxial configuration

The standard equations applied in this scenario to calculate shear and normal stress on the plane of the fracture in Figure 45 are:

$$\sigma_n = \sigma_3 + (\sigma_1 - \sigma_3)sin^2(\theta) \qquad (3-10)$$

$$\tau = (\sigma_1 - \sigma_3)\sin(\theta)\cos(\theta) \qquad (3-11)$$

Applying these equations to the problem in Figure 45:

$$\sigma_n = \sigma_3 + (\sigma_1 - \sigma_3)sin^2(\theta) = 1000 + (4000)sin^2(40) = 2652.7\ psi \qquad (3-12)$$

$$\tau = (\sigma_1 - \sigma_3)\sin(\theta)\cos(\theta) = (4000)\sin(40)\cos(40) = 1969.6\,psi \qquad (3-13)$$

The normal stress is 2652.7 psi and the shear stress is 1969.6 psi. However, horizontal stresses at the FORGE site are not equal. To accommodate this, the stress tensor (equation 3-25) is rotated such that the σ_{zz} component is normal to the plane of the fracture making the outward positive unit normal consist only of a positive z-component. Assume σ_h corresponds to the x-axis, σ_H corresponds to the y-axis and σ_v corresponds to the z-axis. First σ_h (x-axis) is rotated around the z-axis to the dip azimuth of the fracture, then σ_v (z-axis) is rotated about the y-axis (σ_H) to the dip angle of the fracture:

$$\sigma_{kl} = \begin{bmatrix} \sigma_{xx} & \sigma_{xy} & \sigma_{xz} \\ \sigma_{yx} & \sigma_{yy} & \sigma_{yz} \\ \sigma_{zx} & \sigma_{zy} & \sigma_{zz} \end{bmatrix} \qquad (3-14)$$

$$\sigma'_{ij} = a_{ij}\sigma_{kl}a_{kl} \qquad (3-15)$$

Where a_{ij} is the rotation matrix, a_{kl} is the transpose of the rotation matrix, σ_{kl} is the original second rank stress tensor and σ'_{ij} is the rotated tensor in the frame of the fracture plane. The unit normal in the new frame of reference is (0,0,1) which simplifies the calculations of the normal and shear stress magnitudes on the fracture planes. To demonstrate that this method yields the proper values, it is applied to the scenario shown in Figures 44 and 45. The stress tensor for the example is:

$$\sigma_{kl} = \begin{bmatrix} 1000\,psi & 0 & 0 \\ 0 & 1000\,psi & 0 \\ 0 & 0 & 5000\,psi \end{bmatrix} \qquad (3-16)$$

Rotation is only required about the y-axis since horizontal stresses are the same. The rotation matrix rotates the tensor 50° onto the plane of the fracture:

$$a_{ij} = \begin{bmatrix} \cos(50) & 0 & \sin(50) \\ 0 & 1 & 0 \\ -\sin(50) & 0 & \cos(50) \end{bmatrix} \qquad (3-17)$$

$$\sigma'_{ij} = \begin{bmatrix} 0.64 & 0 & 0.77 \\ 0 & 1 & 0 \\ -0.77 & 0 & 0.64 \end{bmatrix} \begin{bmatrix} 1000 & 0 & 0 \\ 0 & 1000 & 0 \\ 0 & 0 & 50 \end{bmatrix} \begin{bmatrix} 0.64 & 0 & -0.77 \\ 0 & 1 & 0 \\ 0.77 & 0 & 0.64 \end{bmatrix} = \begin{bmatrix} 3347\text{ psi} & 0 & 1970\text{ psi} \\ 0 & 1000\text{ psi} & 0 \\ 1970\,psi & 0 & 2654\,psi \end{bmatrix} \qquad (3-18)$$

The unit normal vector is now given by:

$$n = (0,0,1) \qquad (3-19)$$

And the magnitude of the normal stress component on the facture is given by:

$$\sigma_n = \begin{bmatrix} \sigma_{xx} & \sigma_{xy} & \sigma_{xz} \\ \sigma_{yx} & \sigma_{yy} & \sigma_{yz} \\ \sigma_{zx} & \sigma_{zy} & \sigma_{zz} \end{bmatrix} \begin{bmatrix} n_1 \\ n_2 \\ n_3 \end{bmatrix} \begin{bmatrix} n_1 \\ n_2 \\ n_3 \end{bmatrix} \qquad (3-20)$$

Which simplifies to:

$$\sigma_n = \sigma_{xx}n_1^2 + \sigma_{yy}n_2^2 + \sigma_{zz}n_3^2 + 2\left(\sigma_{xy}n_1n_2 + \sigma_{yz}n_2n_3 + \sigma_{xz}\,n_1n_3\right) \qquad (3-20)$$

Applying the matrix equation:

$$\sigma_n = \begin{bmatrix} 3347 & 0 & 1970 \\ 0 & 1000 & 0 \\ 1970 & 0 & 2654 \end{bmatrix} \begin{bmatrix} 0 \\ 0 \\ 1 \end{bmatrix} \begin{bmatrix} 0 \\ 0 \\ 1 \end{bmatrix} = 2654.4\,psi \qquad (3-21)$$

To calculate the shear stress magnitude, first the stress vector on the fracture is calculated:

$$T = \begin{bmatrix} \sigma_{xx} & \sigma_{xy} & \sigma_{xz} \\ \sigma_{yx} & \sigma_{yy} & \sigma_{yz} \\ \sigma_{zx} & \sigma_{zy} & \sigma_{zz} \end{bmatrix} \begin{bmatrix} n_1 \\ n_2 \\ n_3 \end{bmatrix} \qquad (3-22)$$

$$T = \begin{bmatrix} 3347 & 0 & 1970 \\ 0 & 1000 & 0 \\ 1970 & 0 & 2654 \end{bmatrix} \begin{bmatrix} 0 \\ 0 \\ 1 \end{bmatrix} = (1970{,}0{,}2654) \qquad (3-23)$$

Finally, the magnitude of the normal component squared is subtracted from the magnitude of the stress vector:

$$\tau = \sqrt{T_1^2 + T_2^2 + T_3^2 - \sigma_n^2} = 1970\,psi \qquad (3-24)$$

The normal and shear stress magnitudes calculated by rotating the tensor to the plane of the fracture are the same as those calculated by resolving the stresses onto the fracture in the 2D problem in Figure 45. The 3D method of tensor rotation is applied to the fractures in MU-ESW1.

Since the reservoir will be developed in the bottom section of MU-ESW1, the fractures in the interval from 7000-7500 ft will be used to assess stimulation potential. The average overburden in this interval is 7752 psi, average minimum horizontal stress is 4275 psi (EGI, 2018), average maximum horizontal stress is 4700 psi, and average pore pressure is 3143 psi. The minimum horizontal stress strikes at about 115 degrees and the maximum horizontal stress strikes at about 25 degrees. The stress tensor for this configuration is given below:

$$\sigma_{kl} = \begin{bmatrix} 4275 & 0 & 0 \\ 0 & 4700 & 0 \\ 0 & 0 & 7752 \end{bmatrix} \qquad (3-25)$$

The normal stress σ_n and shear stress τ due to the stress tensor are then calculated on each fracture in the study using the procedure to estimate stress states on fractures in 3D. The joints are granite and range from smooth to rough (Faulder, 1991). A failure criterion that considers roughness is (Barton, 1976):

$$\tau_f = \left(\sigma_n - P_p\right) \tan\left(\varphi_b + JRC log_{10}\left(\frac{JCS}{\sigma_n - P_p}\right)\right) \qquad (3-26)$$

The frictional strength of the joint is τ_f, $\left(\sigma_n - P_p\right)$ is the effective normal stress, φ_b is the friction angle of a smooth joint surface 31-33 for wet coarse-grained granite (Coulson, 1972). Here 32 degrees will be used for φ_b. JCS is the joint wall compressive strength which is taken to be the UCS in most cases (here 121 MPa in Table 2). JRC is the joint roughness coefficient given by (Alameda-Hernandez et al., 2014):

$$JRC = 64.22Z_2 - 2.31 \qquad (3-27)$$

Where the parameter Z_2 is the first derivative root mean square. Alameda-Hernandez et al. (2014) estimate the JRC for granite to be 9.5-6.7 which yields a range of possible failure envelopes. Plotting these two possible extremes of the failure envelope with the fracture data gives the plot in Figure 46.

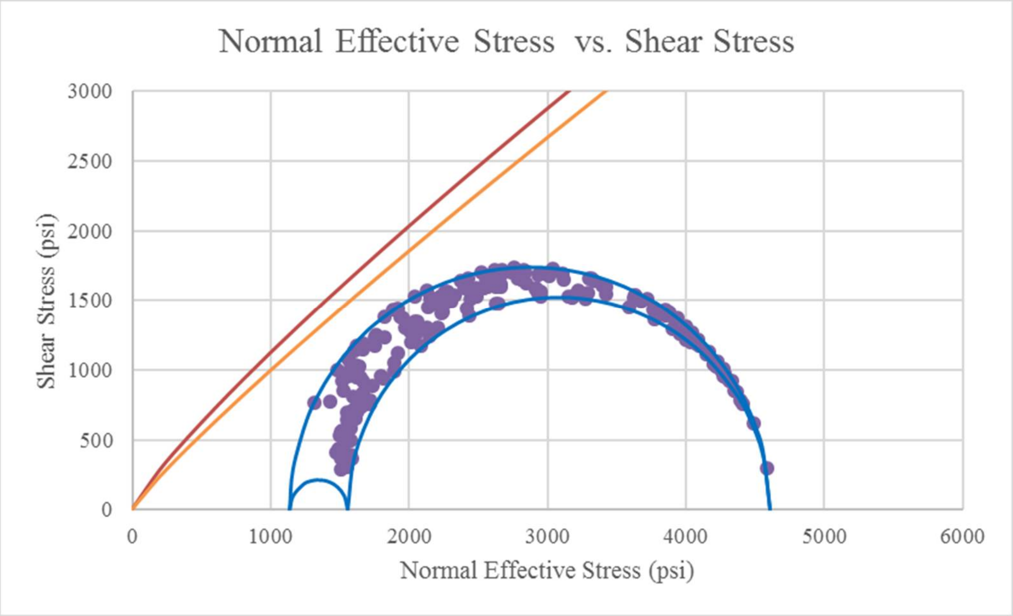

Figure 46: Normal effective and shear stresses on all fractures from the 7000-7500 ft interval in MU-ESW1 plotted in their 3D stress states (purple points). Tensile induced fractures are excluded. Possible ranges of the frictional shear strength envelope (red line is for JRC=9.5 and yellow line is for JRC=6.7) demonstrate the increase in pore pressure needed to cause slip on the most optimally oriented fractures

Given the scenario in Figure 46, it is clear that a range of pore pressure increases may cause sliding since the frictional resistance to slip depends on the roughness. The minimum pore pressure increase required to cause shear applying the lower envelope (JRC=6.7) is about 375 psi shown in Figure 48 and the maximum pore pressure increase required to cause slip based on JRC=9.5 (upper envelope) is about 550 psi as shown in Figure 47. This indicates favorable stimulation conditions at reservoir depths in the FORGE site.

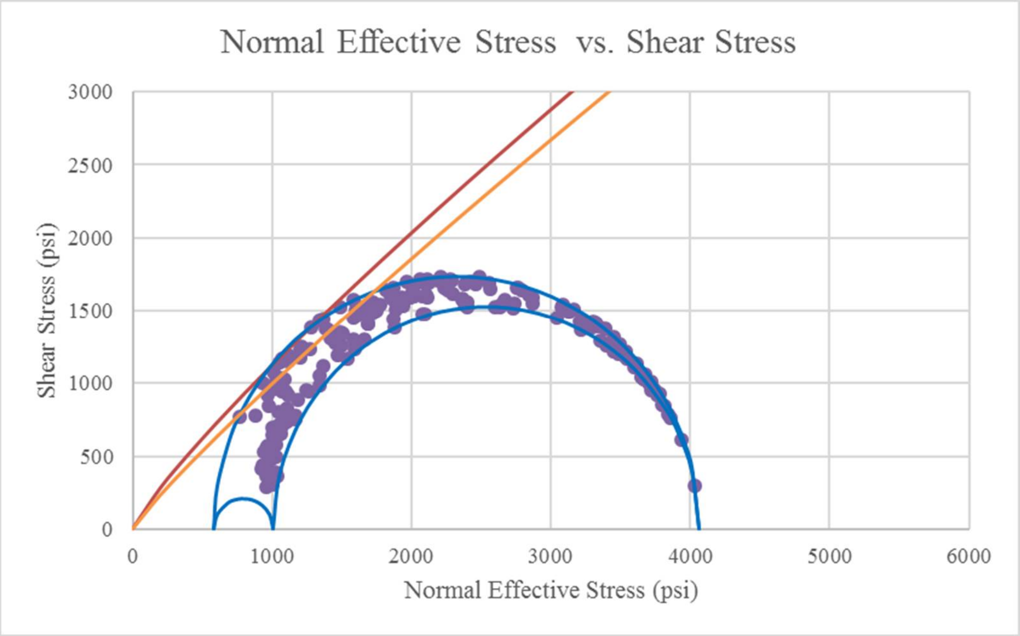

Figure 47: JRC=9.5 (upper red line); fractures touching outer frictional envelope with the increase in in-situ pore pressure of 550 psi. Plot includes all fractures from the bottom 500 ft interval in MU-ESW1

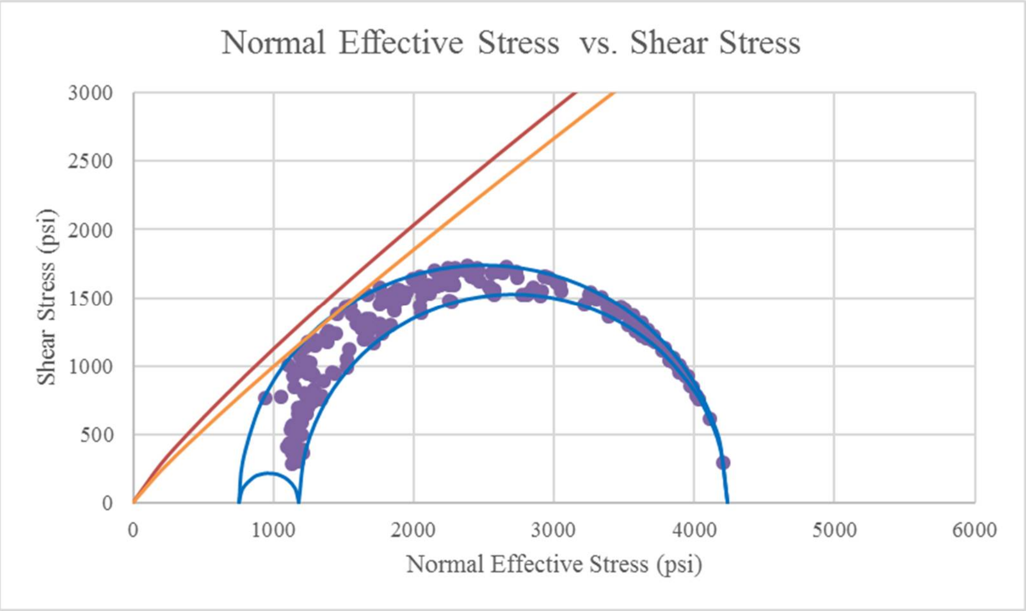

Figure 48: JRC=6.7 (orange line); fractures touching outer frictional envelope with the increase in in-situ pore pressure of 375 psi. Plot includes all fractures from the bottom 500 ft interval in MU-ESW1

Conclusion and Summary

The following conclusions can be drawn from this thesis:

1. The FORGE Utah site resides in a favorable stress field for stimulation.
2. The stresses are well constrained by the injection test and well data.
3. Stress directions seem to vary slightly over the depth of MU-ESW1 but not enough to cause concern for stimulation operations.
4. Increasing pore pressure by about 375-550 psi will cause slip in the most favorably oriented fractures at reservoir depths in the absence of sealing material.
5. Properties across the region are relatively homogenous

References

1. Afsari, M., Ghafoori, M., Roostaeian, M., Haghshenas, A., Ataei, A., & Masoudi, R. (2009, January 1). Mechanical Earth Model (MEM): An Effective Tool for Borehole Stability Analysis and Managed Pressure Drilling (Case Study). Society of Petroleum Engineers. doi:10.2118/118780-MS.

2. Alameda-Hernández, Pedro, Jorge Jiménez-Perálvarez, José A. Palenzuela, Rachid El Hamdouni, Clemente Irigaray, Miguel A. Cabrerizo, and José Chacón. "Improvement of the JRC calculation using different parameters obtained through a new survey method applied to rock discontinuities." *Rock mechanics and rock engineering* 47, no. 6 (2014): 2047-2060.

3. Allis, Rick, Joe Moore, Nick Davatzes, Mark Gwynn, Christian Hardwick, Stefan Kirby, John McLennan, Kris Pankow, Stephen Potter, and Stuart Simmons. "EGS concept testing and development at the Milford, Utah FORGE site." In *Proceedings*. 2016.

4. Arabasz, Walter J., and Dale R. Julander. "Geometry of seismically active faults and crustal deformation within the Basin and Range-Colorado Plateau transition in Utah." *Geological Society of America Special Papers* 208 (1986): 43-74.

5. Bakshi, R., Halvaei, M. E., & Ghassemi, A. (2016), Geomechanical Characterization of Core from the Proposed FORGE Laboratory on the Eastern Snake River Plain, Idaho.

6. Baria, Roy, Jörg Baumgärtner, Fritz Rummel, Robert J. Pine, and Yoshiteru Sato. "HDR/HWR reservoirs: concepts, understanding and creation." *Geothermics* 28, no. 4 (1999): 533-552.

7. Barker, Craig Alan. "Upper-crustal structure of the Milford Valley and Roosevelt Hot Springs, Utah region: by modeling of seismic refraction and reflection data." PhD diss., Department of Geology and Geophysics, University of Utah, 1986.

8. Barton, C. A., Moos, D., Hartley, L., Baxter, S., Foulquier, L., Holl, H., ... & Brisbane, A. U. (2013, February). Geomechanically coupled simulation of flow in fractured reservoirs. In *Proceedings, Thirty-Eighth Workshop on Geothermal Reservoir Engineering, Stanford Univ., Stanford, Calif*.

9. Barton, Nick. "The shear strength of rock and rock joints." In *International Journal of rock mechanics and mining sciences & Geomechanics abstracts*, vol. 13, no. 9, pp. 255-279. Pergamon, 1976.

10. Blackwell, David D., Petru T. Negraru, and Maria C. Richards. "Assessment of the enhanced geothermal system resource base of the United States." *Natural Resources Research* 15, no. 4 (2006): 283-308.

11. Blanton, T. L., and J. E. Olson. "Stress magnitudes from logs: effects of tectonic strains and temperature." In *SPE Annual Technical Conference and Exhibition*. Society of Petroleum Engineers, 1997.

12. Brown, Donald W., David V. Duchane, Grant Heiken, and Vivi Thomas Hriscu. *Mining the earth's heat: hot dry rock geothermal energy*. Springer Science & Business Media, 2012.

13. Bruhn, Ronald L., Michael R. Yusas, and Fernando Huertas. "Mechanics of low-angle normal faulting: an example from Roosevelt Hot Springs geothermal area, Utah." *Tectonophysics*86, no. 4 (1982): 343-361.

14. Bujakowski, Wiesław, Antoni Barbacki, Maciej Miecznik, Leszek Pająk, Robert Skrzypczak, and Anna Sowiżdżał. "Modelling geothermal and operating parameters of EGS installations in the lower triassic sedimentary formations of the central Poland area." *Renewable Energy* 80 (2015): 441-453.

15. Cheng, Qinglu, and Ahmad Ghassemi. "Numerical Modeling of Newberry EGS Stimulation." In *50th US Rock Mechanics/Geomechanics Symposium*. American Rock Mechanics Association, 2016.

16. Coleman, Drew S., John M. Bartley, J. Douglas Walker, David E. Price, and Anke M. Friedrich. "Extensional faulting, footwall deformation and plutonism in the Mineral Mountains, Southern Sevier Desert." *Brigham Young University Geology Studies* 42, no. 2 (1997): 203-233.

17. Coulson, James H. "Shear strength of flat surfaces in rock." In *Stability of Rock Slopes*, pp. 77-105. ASCE, 1972.

18. Economides, Michael J., and Kenneth G. Nolte. *Reservoir stimulation*. Vol. 2. Englewood Cliffs, New Jersey: Prentice Hall, 1989.

19. EGI at the University of Utah. *Frontier Observatory for Research in Geothermal Energy Milford Site, Utah*. No. DOE DE-EE0007080. University of Utah, Salt Lake City (USA). EGI, 2018.

20. Eissa, E. A., and A. Kazi. "Relation between static and dynamic Young's moduli of rocks." In *International Journal of Rock Mechanics and Mining Sciences & Geomechanics Abstracts*, vol. 25, no. 6, pp. 479-482. Pergamon, 1988.

21. Evans Jr, S. H., and William P. Nash. "Quaternary Rhyolite from the Mineral Mountains, Utah, USA." *US Government Documents (Utah Regional Depository)* (1978): 597.

22. Faulder, D. D. "Long-Term Flow Test# 1, Roosevelt Hot Springs, Utah." *US Government Documents (Utah Regional Depository)* (1994): 589.

23. Faulder, D. D. *Conceptual geologic model and native state model of the Roosevelt Hot Springs hydrothermal system*. Idaho National Engineering Laboratory, 1991.

24. Frydman, M. "Determinations of the dynamic elastic constants of a transverse isotropic rock based on borehole dipole sonic anisotropy in deviated wells." In *Rio Oil and Gas Expo and Conference, IBP2304_10*. 2010.

25. Gertson, Rodney Curtis, and Robert B. Smith. *Interpretation of a seismic refraction profile across the Roosevelt Hot Springs, Utah and vicinity*. No. IDO-78-1701. a. 3. Utah Univ., Salt Lake City (USA). Dept. of Geology and Geophysics, 1979.

26. Gringarten, Emmanuel, and Clayton V. Deutsch. "Teacher's aide variogram interpretation and modeling." *Mathematical Geology* 33, no. 4 (2001): 507-534.

27. Gwynn, Mark, Rick Allis, Christian Hardwick, Jay Hill, and Joe Moore. "A new look at the thermal regime around Roosevelt Hot Springs, Utah." *Geothermal Resources Council Transactions* 40 (2016): 551-558.

28. Hardwick, C. L., Mark Gwynn, Rick Allis, Phillip Wannamaker, and Joe Moore. "Geophysical signatures of the Milford, Utah FORGE site." In *41st Workshop on Geothermal Reservoir Engineering*, vol. 11. 2016.

29. Hemami, Behzad, and Ahmad Ghassemi. "A Study of Basement Structures in Central Oklahoma with Reference to Seismicity." In *52nd US Rock Mechanics/Geomechanics Symposium*. American Rock Mechanics Association, 2018.

30. Ide, John M. "Comparison of statically and dynamically determined Young's modulus of rocks." *Proceedings of the National Academy of Sciences* 22, no. 2 (1936): 81-92.

31. Jaeger, J. C., Cook, N. G., & Zimmerman, R. (2009). *Fundamentals of rock mechanics*. John Wiley & Sons.

32. Kamali, A., and A. Ghassemi. "Reservoir Stimulation in Naturally Fractured Poroelastic Rocks." In *51st US Rock Mechanics/Geomechanics Symposium*. American Rock Mechanics Association, 2017.

33. Keys, W. Scott. "Borehole geophysics in igneous and metamorphic rocks." *The Log Analyst* 20, no. 04 (1979).

34. King, M. Soo. "Static and dynamic elastic properties of rocks from the Canadian Shield." In *International Journal of Rock Mechanics and Mining Sciences & Geomechanics Abstracts*, vol. 20, no. 5, pp. 237-241. Pergamon, 1983.

35. Kirsch, G. (1898). Die theorie der elastizität und die bedürfnisse der festigkeitslehre. Springer.

36. Kraft, Toni, Paul Martin Mai, Stefan Wiemer, Nicholas Deichmann, Johannes Ripperger, Philipp Kästli, Corinne Bachmann, Donat Fäh, Jochen Wössner, and Domenico Giardini. "Enhanced geothermal systems: Mitigating risk in urban areas." *Eos, Transactions American Geophysical Union* 90, no. 32 (2009): 273-274.

37. Lai, Goh Thian, Abdul Ghani Rafek, Ailie Sofyiana Serasa, Norbert Simon, Lee Khai Ern, and A. Hussain. "Empirical correlation of uniaxial compressive strength and primary wave velocity of Malaysian granites." *The Electronic Journal of Geotechnical Engineering E* 19 (2014): 1063-1072.

38. Liu, Jiman. "Geomechanical Reservoir Characterization and Applications." A Thesis Approved for the University of Oklahoma Mewbourne School of Petroleum and Geological Engineering. University of Oklahoma, 2017.

39. Moos, D., & Zoback, M. D. (1990). Application to Continental, Deep Sea Drilling Project, and. *Journal of Geophysical Research*, *95*(B6), 9305-9325.

40. Moos, D., and C. A. Barton. "In-situ stress and natural fracturing at the INEL site, Idaho." (1990).

41. Moos, Daniel, and Mark D. Zoback. "Utilization of observations of well bore failure to constrain the orientation and magnitude of crustal stresses: application to continental, Deep Sea Drilling Project, and Ocean Drilling Program boreholes." *Journal of Geophysical Research: Solid Earth* 95, no. B6 (1990): 9305-9325.

42. Najibi, A. R., Ghafoori, M., Lashkaripour, G. R., & Asef, M. R. (2015). Empirical relations between strength and static and dynamic elastic properties of Asmari and Sarvak limestones, two main oil reservoirs in Iran. *Journal of Petroleum Science and Engineering*, *126*, 78-82.

43. Nielson, Dennis L. "Stress in geothermal systems." *Geothermal Resources Council Transactions* 13 (1989): 271-276.

44. Nielson, Dennis L., Stanley H. Evans, and Bruce S. Sibbett. "Magmatic, structural, and hydrothermal evolution of the Mineral Mountains intrusive complex, Utah." *Geological Society of America Bulletin* 97, no. 6 (1986): 765-777.

45. Nygren, A., and A. Ghassemi. "Influence of cold water injection on critically stressed fractures in Coso geothermal field, CA." In *Alaska Rocks 2005, The 40th US Symposium on Rock Mechanics (USRMS)*. American Rock Mechanics Association, 2005.'

46. Oyler, D. C., Mark, C., & Molinda, G. M. (2010). In situ estimation of roof rock strength using sonic logging. *International Journal of Coal Geology*,*83*(4), 484-490.

47. Pine, R. J., and A. S. Batchelor. "Downward migration of shearing in jointed rock during hydraulic injections." In *International Journal of Rock Mechanics and Mining Sciences & Geomechanics Abstracts*, vol. 21, no. 5, pp. 249-263. Pergamon, 1984.

48. Plumb, R., Edwards, S., Pidcock, G., Lee, D., & Stacey, B. (2000, January). The mechanical earth model concept and its application to high-risk well construction projects. In *IADC/SPE Drilling Conference*. Society of Petroleum Engineers.

49. Pratt, H.R. and Simonson, E.R., 1976. "Geotechnical studies of geothermal reservoirs." *Report to Energy Resources Development Agency*, pp. 30-34.

50. Rahman, M. K., M. M. Hossain, and S. S. Rahman. "A shear-dilation-based model for evaluation of hydraulically stimulated naturally fractured reservoirs." *International Journal for Numerical and Analytical Methods in Geomechanics* 26, no. 5 (2002): 469-497.

51. Ross, Howard P., Dennis L. Nielson, and Joseph N. Moore. "Roosevelt Hot Springs Geothermal System, Utah--Case Study." *AAPG Bulletin* 66, no. 7 (1982): 879-902.

52. Schellschmidt, Rüdiger, Burkhard Sanner, Sandra Pester, and Rüdiger Schulz. "Geothermal energy use in Germany." In *Proceedings World geothermal congress*, vol. 152, p. 19. 2010.

53. Shannon Jr, Spencer S., Roland Pettitt, John Rowley, Fraser Goff, Mark Mathews, and Jimmy J. Jacobson. *Acord 1-26 hot, dry well, Roosevelt Hot Springs hot dry rock prospect, Utah*. No. LA-9857-HDR. Los Alamos National Lab., NM (USA), 1983.

54. Sibbett, Bruce S. and Dennis L. Nielson. “Geologic map of the central mineral mountains (GIS of 1980 map), Beaver County, Utah. 2017.

55. Simmons, Stuart, Stefan Kirby, Clay Jones, Joe Moore, Rick Allis, Adam Brandt, and Greg Nash. "The Geology, Geochemistry, and Geohydrology of the FORGE Deep Well Site, Milford, Utah."

56. Smith, Robert B., and Ronald L. Bruhn. "Intraplate extensional tectonics of the eastern Basin-Range: Inferences on structural style from seismic reflection data, regional tectonics, and thermal-mechanical models of brittle-ductile deformation." *Journal of Geophysical Research: Solid Earth* 89, no. B7 (1984): 5733-5762.

57. Sowiżdżał, A., Bartosz Papiernik, Grzegorz Machowski, and Marek Hajto. "Petrophysical parameters of the Lower Triassic deposits in prospective location for Enhanced Geothermal System (central Poland)." *Geological Quarterly* 57, no. 4 (2013): 729-744.

58. Spence, G. H., Couples, G. D., Bevan, T. G., Aguilera, R., Cosgrove, J. W., Daniel, J. M., & Redfern, J. (2014). Advances in the study of naturally fractured hydrocarbon reservoirs: a broad integrated interdisciplinary applied topic. *Geological Society, London, Special Publications*, *374*(1), 1-22.

59. Takarli, Mokhfi, and William Prince-Agbodjan. "Temperature effects on physical properties and mechanical behavior of granite: experimental investigation of material damage." *Journal of ASTM International* 5, no. 3 (2008): 1-13.

60. Tester, Jefferson W., Brian J. Anderson, Anthony S. Batchelor, David D. Blackwell, Ronald DiPippo, E. Drake, John Garnish et al. "The future of geothermal energy: Impact of enhanced geothermal systems (EGS) on the United States in the 21st century." *Massachusetts Institute of Technology* 209 (2006).

61. Wang, J., Jung, W., Li, Y., & Ghassemi, A. (2016). Geomechanical characterization of Newberry Tuff. *Geothermics*.

62. Wang, Z. (2000). Dynamic versus static elastic properties of reservoir rocks. Seismic and Acoustic Velocities in Reservoir Rocks, SEG Geophysics Reprint Series, No. 19.

63. Wannamaker, Philip E., William R. Sill, and Stanley H. Ward. "MAGNETOELLURIC OBSERVATIONS AT THE ROOSEVELT HOT SPRINGS KGRA AND MINERAL MTS, UTAH." In *Geotherm Resour Counc, Annu Meet, Geotherm Energy-A Novelty Becomes Resour*. Geotherm Resour Counc (Trans, v 2), 1978.

64. Ward, Stanley H., and Terry Joseph Crebs. *Report on Preliminary Resistivity Survey, Roosevelt Hot Springs KRGA*. University of Utah, Department of Geology and Geophysics, 1975.

65. Wiebols, G. A., and N. G. W. Cook. "An energy criterion for the strength of rock in polyaxial compression." In *International Journal of Rock Mechanics and Mining Sciences & Geomechanics Abstracts*, vol. 5, no. 6, pp. 529-549. Pergamon, 1968.

66. Willis-Richards, J., K. Watanabe, and H. Takahashi. "Progress toward a stochastic rock mechanics model of engineered geothermal systems." *Journal of Geophysical Research: Solid Earth* 101, no. B8 (1996): 17481-17496.

67. Yarus, J. M., & Chambers, R. L. (2006). Practical geostatistics-an armchair overview for petroleum reservoir engineers. *Journal of Petroleum Technology*, *58*(11), 78-86.

68. Ye, Zhi, Michael Janis, and Ahmad Ghassemi. "Injection-driven Shear Slip and The Coupled Permeability Evolution of Granite Fractures for EGS Stimulation." In *51st US Rock Mechanics/Geomechanics Symposium*. American Rock Mechanics Association, 2017.

69. Yusas, Michael Ray, and Ronald L. Bruhn. *Structural fabric and in-situ stress analyses of the Roosevelt Hot Springs KGRA*. No. DOE/ET/28392-31. Utah Univ., Salt Lake City (USA). Dept. of Geology and Geophysics, 1979.

70. Zoback, Mark D. *Reservoir geomechanics*. Cambridge University Press, 2010.